OXFORD

Journal of Petrology, 2022, **63**, 1–23
https://doi.org/10.1093/petrology/egac059
Original Manuscript

Zircon Reveals Diverse Trends of Magma Crystallization from Two Types of Early Post-Collisional Diorites (Variscan Orogen, NE Bohemian Massif)

Anna Pietranik[1,*], Federico Farina[2], Katarzyna Derkowska[1,3], Urs Schaltegger[4], Arkadiusz Przybyło[1], Craig Storey[5], Stephanie Lasalle[5], Bruno Dhuime[6], Magdalena Pańczyk[3], Grzegorz Zieliński[3], Małgorzata Nowak[1], Kamil Bulcewicz[1] and Jakub Kierczak[1]

[1]University of Wrocław, Institute of Geological Sciences, Borna 9, 50-204, Wrocław, Poland;
[2]Department of Earth Sciences, University of Milano, Via Botticelli, 23, 20133 Milano, Italy;
[3]Polish Geological Institute, Rakowiecka 4, 00-975, Warsaw, Poland;
[4]Department of Earth Sciencesa, University of Geneva, rue des Maraîchers 13, CH-1205 Genève, Switzerland;
[5]University of Portsmouth, School of Earth and Environmental Sciences, Burnaby Building, Burnaby Road, PO1 3QL, Portsmouth, UK; and
[6]Deptertment of Earth Sciences, University of Bristol, Wills Memorial Building, Queen's Road, BS8 1RJ, Bristol, UK

*Corresponding author. Telephone: Tel: +48713759296. Fax: +48713759371. E-mail: anna.pietranik@uwr.edu.pl.

Abstract

Amphibole- and clinopyroxene-bearing monzodiorites were emplaced at 340 Ma (CA-ID-TIMS zircon age), suggesting the formation of hydrous and dry magmas closely related in space and time in the NE Bohemian Massif. Hafnium and oxygen isotopes of zircon in less evolved rocks (<55 wt% SiO2) are similar between Amp and Cpx monzodiorites (εHf = −3.3 ± 0.5 and − 3.5 ± 0.8; δ^{18}O = 6.4 ± 1.0 and 6.8 ± 0.7, respectively), consistent with a common source—a contaminated mafic magma derived from an enriched mantle. At the same time, the conditions of crystallization are distinct and zircon appears to be an excellent tool for distinguishing between hydrous and anhydrous crystallization conditions, a process that may be more ambiguously recorded by whole rock and major mineral chemistry. In particular, elements fractionated by either amphibole or plagioclase crystallization, such as Hf, Dy, and Eu, differ in zircon from amphibole- and clinopyroxene-bearing rocks, and Zr/Hf, Yb/Dy, and Eu/Dy are therefore useful indices of crystallization conditions. We show that the composition of zircon from hydrous dioritic magmas is not comparable with that of typical zircon from dioritic-granitic suites worldwide, suggesting a specific process involved in their formation. Here, we propose that fluid-present remelting of a mafic underplate is necessary to explain the rock textures as well as the composition of the whole rock, zircon, and other minerals of amphibole-bearing monzodiorites and that a similar process may control the formation of amphibole-rich dioritic rocks worldwide, including appinitic suites. Overall, we show that dioritic rocks represent snapshots of differentiation processes that occur in the early stages of magma evolution before the magma is homogenized into large-scale batholiths.

INTRODUCTION

The importance of fluids contributing to magma formation within the continental crust has lately regained considerable interest (e.g. Weinberg & Hasalová, 2015; Clemens *et al.*, 2021; Collins *et al.*, 2021). Water-rich fluids may be a prerequisite for many processes that control magma composition and productivity (Collins *et al.*, 2020b); however, whether the presence of such fluids is essential for arc magma formation is disputed (Clemens *et al.*, 2021). In the continental crust, for example, appinites (plutonic rocks containing idiomorphic hornblende) represent mafic to intermediate magmas that are undoubtedly enriched in water (Murphy, 2013, 2020). Based on the O and H isotope composition of amphibole, the water in appinites is mantle-sourced, but a crustal contribution cannot be excluded (Cawood *et al.*, 2021). Therefore, appinites (or related rocks such as durbachites and vaugnerites), despite being much less voluminous than more evolved granitic magmas, provide important records of metasomatically enriched mantle magma and its contamination by crustal melts (Janoušek *et al.*, 2020; Bea *et al.*, 2021). As such, they may provide insight into the presence and nature of fluids in the lithosphere.

The collision between Gondwana and Laurussia at 410–300 Ma formed an enriched mantle source, characterized by negative εNd, consistent with mantle interaction with subduction-derived fluids/melts (Dostal *et al.*, 2019, 2020). The area studied in this paper (NE Bohemian Massif) offers insight into the formation of water-rich magmas related to this collision in a complex, early-stage post-collisional setting at ca. 340 Ma. Six episodes of magmatic activity were identified in the Bohemian Massif from 375 Ma to 296 Ma, with the ca. 340 Ma episode marking a distinct change from active-margin, continental arc to post-collisional magmatism

Received: February 16, 2021. **Revised:** June 20, 2022. **Accepted:** June 21, 2022

(Žák *et al.*, 2014; Trubač *et al.*, 2020). This change is also reflected in the magma sources that evolved from mantle-dominated toward crustal (Trubač *et al.*, 2020). Also, magmatism at ca. 340 Ma involved emplacement of high-potassic to ultrapotassic magmas with a suspected metasomatized, lithospheric mantle source (Janoušek *et al.*, 2020). In this study, we focus on comparing mineral records and crystallization age of ca. 340 Ma amphibole-rich and clinopyroxene-rich high-potassic to shoshonitic rocks that occur in close association in the NE Bohemian Massif. Consistent with the experimental results for mafic to intermediate magma crystallization (Melekhova *et al.*, 2015, 2017; Ulmer *et al.*, 2018) these intrusions should represent water-rich and water-poor magmas, respectively, formed in close association during the orogenic collapse. The aim is to understand the role of water in producing magmas with distinct mineral compositions and place these diverse magmas in the context of post-collisional processes. The NE Bohemian Massif represents a complex tectonic setting where up to three fault-bounded crustal blocks have been identified (Jastrzębski *et al.*, 2020; Szczepański *et al.*, 2021). We discriminate the contributions from these sources using the geochemical and isotopic composition of the studied rocks, as well as the chemical composition of major and accessory minerals. The combined isotopic and trace element compositions of zircon are shown to be particularly sensitive to the evolution of magmas with different water content.

GEOLOGICAL SETTING

The studied rocks are situated in the north-eastern part of the Bohemian Massif (Fig. 1), one of the crustal blocks that consolidated during the Gondwana and Laurasia collision in the course of the 410–300 Ma Variscan Orogeny, which was followed by an extensional period from 300 to 250 Ma (Kroner & Romer, 2013). The Variscan igneous rocks in the Bohemian Massif represent different stages of orogenic development (Žák *et al.*, 2014; Trubač *et al.*, 2020) starting with (1) a suite of ca. 375–340 Ma rocks with typical island arc affinity (Janoušek *et al.*, 2004; Janoušek *et al.*, 2006; Žák *et al.*, 2011), followed by (2) ca. 350–336 Ma potassic to ultrapotassic rocks emplaced during the syn-collisional to the early post-collisional stage (Janoušek & Holub, 2007; Kotková *et al.*, 2010; Oberc-Dziedzic *et al.*, 2015; Maierová *et al.*, 2016; Kubínová *et al.*, 2017; Jokubauskas *et al.*, 2018) and by (3) 326–296 Ma voluminous late post-collisional to post-collapse magmas with both inherited subduction and genuinely intra-continental affinities (Pietranik & Waight, 2008; Słaby & Martin, 2008; Kryza *et al.*, 2012; Laurent *et al.*, 2014; Turniak *et al.*, 2014; Dostal *et al.*, 2020). The general isotopic evolution of magmas shows a secular trend with early magma being dominated by mantle sources and later ones (from 340 Ma on) by crustal ones (Trubač *et al.*, 2020). Particularly interesting are high-potassic to ultrapotassic magmas that intruded at 335–340 Ma and that were derived from strongly metasomatised mantle affected by crustal melts from granulites (Janoušek *et al.*, 2020). Magmas of similar age and composition are present in the NE Bohemian Massif, the Niemcza Zone (NZ)—the focus of this study (Pietranik *et al.*, 2013).

The Variscan collision zone in the NE Bohemian Massif is currently composed of a mosaic of juxtaposed high-grade and low-grade domains (Mazur *et al.*, 2006; Szczepański *et al.*, 2021). The NZ formed close to the border between the Teplá-Barrandian/Bohemian, Saxothuringian and Brunovistulian terranes (Jastrzębski *et al.*, 2020; Szczepański *et al.*, 2021). The NZ is a shear zone (Fig. 1a), which resulted in the mylonitization of the Sowie Mountain gneisses (Puziewicz & Mazur, 1995). The gneisses underwent metamorphism and deformation from 390 Ma to 360 Ma (Jastrzębski *et al.*, 2021). The NZ includes also a serpentinite massif (the Szklary Massif, Fig. 1b) that is probably, but not necessarily, related to the Central Sudetic Ophiolite (Kryza & Pin, 2010; Awdankiewicz *et al.*, 2021). The zone was intruded by intermediate to felsic plutonic rocks at ca. 350–330 Ma (Pietranik *et al.*, 2013; Oberc-Dziedzic *et al.*, 2015). Based on the geological maps, some igneous rocks occur within NZ and some close to NZ within the Sowie Mountain metamorphic rocks (Fig. 1c). Similar shear-related, intermediate to felsic plutonic rocks, emplaced approximately between 350 and 330 Ma, are common in the NE Bohemian Massif and are characterized by overall high-K to shoshonitic composition and typical crustal/arc-like trace-element patterns (Pietranik *et al.*, 2013; Oberc-Dziedzic *et al.*, 2015; Jastrzębski *et al.*, 2018; Jokubauskas *et al.*, 2018). Each location is characterized by distinct Nd and Sr isotope compositions, with Niemcza plutonic rocks being the most primitive ($^{87}Sr/^{86}Sr_i$ ratios of 0.7054–0.7073 and εNd_i values from −1.6 to −3.7; Oberc-Dziedzic *et al.*, 2015).

The Niemcza plutonic rocks are traditionally divided into two groupings: felsic and intermediate (Puziewicz, 1988). The felsic rocks form larger bodies comprising mostly granodiorites/quartz monzonites that commonly contain monzodioritic/dioritic enclaves (Puziewicz, 1992; Pietranik & Koepke, 2014). The intermediate rocks form dykes in metamorphic rocks and consist of diorites, quartz diorites, monzodiorites and quartz monzodiorites (Puziewicz, 1988, 1990; Pietranik *et al.*, 2013).

ANALYTICAL METHODS

Sampling

The dioritic rocks are the focus of this study and are primarily accessible in quarries. Four quarries are established in which the rocks occurring as dykes are extracted, and one quarry is used for extraction of felsic rocks containing enclaves (Pietranik & Koepke, 2014; Przybyło *et al.*, 2022). Only dykes were sampled in this study to avoid *in situ* interactions between granodioritic host and dioritic enclaves. Samples were collected from Przedborowa ($n = 29$), Kluczowa ($n = 2$), Koźmice ($n = 8$)

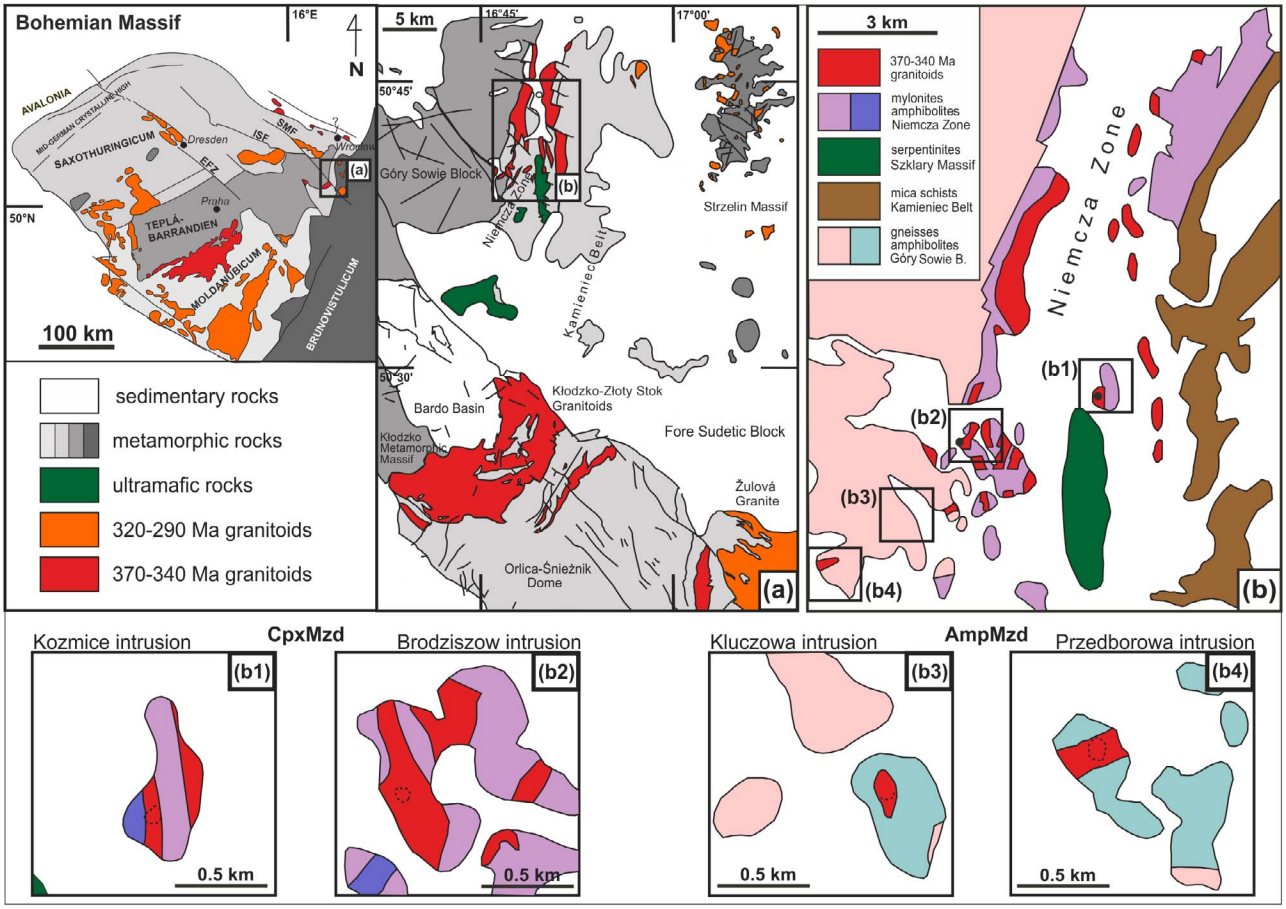

Figure 1. Geological maps of the studied area modified after Sawicki (1995) and Jastrzębski *et al.* (2018), inset shows outline of the Bohemian Massif with terranes boundaries indicated and Variscan granitoids older than 340 Ma shown in red and younger shown in green: (a) schematic map of the NE Bohemian Massif, (b) schematic map of the NZ, (b1–b4) detailed maps of the studied intrusions and surrounding rocks (legend as in b).

and Brodziszów ($n = 5$). Three of these intrusions were previously characterized in detail in Puziewicz (1988), Puziewicz (1990) and Pietranik *et al.* (2013). Kluczowa is a newly opened quarry. A detailed description of the samples and GPS coordinates of the sampling sites are given in the Supplementary Material (Table SM 2.1).

Whole-rock geochemistry

Bulk rock compositions were determined for 14 samples (8 from Przedborowa, and 2 each from Kluczowa, Koźmice and Brodziszów). Whole-rock major and trace element analyses were performed using lithium metaborate–tetraborate fusion by the Bureau Veritas (Vancouver, Canada). Major element compositions were determined by ICP-ES (inductively coupled plasma emission spectrometry). Trace elements were analyzed by ICP-MS (inductively coupled plasma mass spectrometry). The analytical reproducibility (2SD), as estimated from four analyses of standard SO18/CSC and duplicate analysis of a single dioritic sample, is better than 2.2% for major elements, and ranges from 1.6% (Nd) to 29% (Ta) for trace elements at 95% confidence limits. Analytical accuracy (2SD), as estimated from the accepted concentration in the standard SO18/CSC (Table SM1.1) is better than 10% for major elements and better than 40% for trace elements, but mostly better than 15% (calculations are presented in Supplementary Material Table SM1.1). Geochemical data were plotted using GCDKit software (Janoušek *et al.*, 2006).

Electron microprobe

Back-scattered electron (BSE) images, wavelength-dispersive spectroscopy spectra and *in situ* quantitative chemical analyses were carried out using a CAMECA SX-100 electron microprobe in the Micro-Area Analysis Laboratory, Polish Geological Institute in Warsaw, Poland. Data were collected under the following conditions: 15 kV of accelerating voltage, 20–40 nA beam current, with a beam defocused from 1 to 5 μm (to prevent Na and F loss). To minimize interference effects from overlapping X-ray lines, the following corrections were used: Ti-Kα(Ba-Lα_1), Mn-Kα(Cr-Kβ_1), Fe-Kα(Mn-K β_1), V-Kα (Ti-K β_1), Cr-Kα (V-K β_1), Mn-Kα(Cr-K β_1), Fe-Kα(Mn-K β_1), Ce-Lα(Ba-L β_1) (where, e.g., 'Ti-Kα(Ba-Lα_1)' means correction for measured Ti-Kα line, overlapped by Ba-Lα line). Different analytical setups were used to measure the chemical composition of major minerals, zircon, apatite and titanite. The set of analyzed elements with measured lines, diffraction crystals, detection limits of measurements (ppm) and reference standards for each

measured X-ray line are presented in Supplementary Material Table SM1.2 (EMPA).

Zircon analyses

Zircon was separated by hand-picking after several kilos of each sample was crushed, sieved and panned to concentrate heavy minerals. Selected zircon grains were mounted in epoxy resin, polished and observed using an optical microscope (in reflected and transmitted light), then imaged by cathodoluminescence (CL) using a scanning electron microscope. The CL images were used to characterize the zircon grains and choose locations for further *in situ* analyses (Supplementary Material SM3).

CA-ID-TIMS zircon dating

U–Pb Chemical Abrasion Isotope-Dilution Thermal Ionization Mass Spectrometry (CA-ID-TIMS) analysis of zircon grains was carried out at the University of Geneva (Switzerland) using an IsotopX PhoeniX thermal ionization mass spectrometer. The analyses were performed using the EARTHTIME ^{205}Pb-^{233}U-^{235}U tracer solution (ET535; Condon *et al.*, 2015). Accuracy was checked by analyzing the synthetic EARTHTIME ET100 solution (Schaltegger *et al.*, 2021).

High-precision U–Pb dating was done for two samples from amphibole-bearing monzodiorite (CP06) and clinopyroxene-bearing monzodiorite (CK03). The whole zircon grains were analyzed with no control on the presence of possible inherited cores. However, the previous dating by LA-ICP-MS (Pietranik *et al.*, 2013) and CL imagining of numerous zircons during this study (Supplementary Material SM3) did not reveal obvious inherited cores, as expected from magmas with SiO_2 contents of 50–58 wt%. Zircon from AmpMzd forms large crystals up to 500 μm in length. These crystals were chemically abraded, following Widmann *et al.* (2019) to eliminate or attenuate lead loss. The crystals, after being annealed at 900°C for ~48 h, were transferred into 3 ml Savillex beakers, rinsed with 3 N HNO_3 and loaded in HF and trace HNO_3 into 200 μl Savillex microcapsules for partial dissolution (i.e. chemical abrasion) at 210°C for 12 hours. The CpxMzd zircons were smaller than AmpMzd ones and most of them dissolved when subjected to the standard chemical abrasion procedure (performed for 12 hours at 210 OC), therefore the time of abrasion was reduced to 8 hours. All ^{206}Pb/^{238}U data were corrected for initial ^{238}U-^{230}Th disequilibrium assuming that variations in Th/U of analyzed zircons are due to variations in the Th/U of the magma in equilibrium with the zircon using the $D_{(Th)}/D_{(U)}$ value of 0.214 derived from published experimental data (Rubatto & Hermann, 2007).

Trace elements in zircon

Trace-element data were collected using a laser ablation-inductively coupled plasma mass spectrometer (LA-ICP-MS: ASI RESOlutionArF 193 nm laser coupled to an Agilent 7500CS quadrupole mass spectrometer) at the School of Earth and Environmental Sciences at the University of Portsmouth, following the machine set-up described in Pietranik *et al.* (2017). Data were reduced using the Sills software (Guillong *et al.*, 2008). The stoichiometric Zr content in zircon (47.9 wt %) was used as the internal standard, the contents were similar to those estimated in natural minerals using EMP analyses (48.5 ± 0.6 wt% Zr in zircon, $n = 74$). MPI-DING glass and KHAN titanite (Jochum *et al.*, 2006; Heaman, 2009) were analyzed during the session as secondary standards giving good agreement for many trace elements including Rare Earth Elements (REE) concentrations between the measured data and those reported in the literature (Table SM1.3; Ca content was used as an internal standard in both glass and titanite).

Hf isotopes in zircon

Hafnium isotope composition of zircon was measured in five diorite samples ($n = 10$–25) and one granodiorite sample ($n = 10$) using a Thermo-Scientific Neptune MC-ICP-MS (multi-collector inductively coupled plasma mass spectrometer) coupled to a New Wave Research UP193HE Deep-UV (193 nm) ArF Excimer laser ablation sampling system at the University of Bristol (Bristol Isotope Group). Correction for the interferences and mass bias followed the routine of Kemp *et al.* (2006). The correction for the isobaric interference of ^{176}Yb and ^{176}Lu on ^{176}Hf followed the method described in Fisher *et al.* (2011). The accuracy and long-term reproducibility of the measurements were estimated by measuring three zircon reference standards: Plešovice (^{176}Hf/^{177}Hf = 0.282472 ± 16, $n = 27$), Mud Tank (^{176}Hf/^{177}Hf = 0.282504 ± 17, $n = 33$) and Temora II (^{176}Hf/^{177}Hf = 0.282662 ± 22, $n = 27$, all uncertainties at 2 SD level). The values measured for Plešovice, Temora II and Mud Tank are in the agreement with the literature data (Plešovice, 0.282482 ± 13; Temora II, 0.282686 ± 8; Mud Tank, 0.282507 ± 6; Woodhead & Hergt, 2005; Sláma *et al.*, 2008, Table SM1.4).

Oxygen isotopes in zircon

Hand-picked zircons from the five studied samples and several grains of the TEMORA II and 91 500 zircon standards were cast into epoxy mounts.

Oxygen isotope analyses were performed on a SHRIMP II multi-collector ion-microprobe at the Micro-area Analysis Laboratory of PGI-NRI, Warsaw. The configuration of the instrument and applied analytical procedure were based on those described by Ickert *et al.* (2008). A $^{133}Cs^+$ primary ion beam was focused to a diameter of about 23 μm with a sample current of ~3.5 nA. Secondary O− Ions were accelerated by −10 kV with an electron gun (45°) for charge compensation. Two multi-collector Faraday cups (FC) with electrometers equipped with 10^{11} Ω resistors were used to measure ^{16}O and ^{18}O simultaneously. The average intensities of signals were 3.8×10^9 cps for ^{16}O and 7.3×10^6 cps for ^{18}O. Each SHRIMP-II analysis consisted of two series of six scans. EISIE (electron-inducted secondary ion emission) was measured before the analysis and between series. The total counting time

for each analytical spot was about 7 min. Generally, the reference material TEMORA II was analyzed two times, at the beginning and end of each session, and after every three unknowns during the whole session. The 91500 zircon standard was analyzed as the secondary standard and the value measured (avg. $\delta^{18}O = 9.9 \pm 0.7$, $n = 17$, Table SM1.5) are in the agreement with the literature data $\delta^{18}O = 9.9 \pm 0.3$ (Wiedenbeck *et al.*, 2004).

The oxygen isotope data were reduced and corrected using the POXI MC software, which applied background EISIE (Ickert *et al.*, 2008) and corrected for potential drift. Oxygen isotope ratios are reported in standard permil notation relative to Vienna Standard Mean Ocean Water.

MELTS modeling

The MELTS-rhyolite v.1.2.0 software package (Gualda *et al.*, 2012; Ghiorso & Gualda, 2015) was applied to model the affinity of TiO_2 and SiO_2 in the melt along with its evolution from liquidus to solidus following the approach described by Schiller & Finger (2019). The affinities were recalculated to activities and used in the Ti-in-zircon temperature calculations. As starting compositions, bulk-rock chemistries of amphibole-bearing monzodiorite (CP12) and clinopyroxene-bearing monzodiorite (CK04) were used as they are interpreted to represent melt compositions. We ran simulations as one-stage equilibrium crystallization models under isobaric conditions (3 kbar). Oxygen fugacity was set to FMQ-1 (fayalite-magnetite-quartz) buffer for CpxMzd and FMQ + 2 for AmpMzd (the choice of the parameters is based on the thermobarometer for amphibole and the oxymeters for zircon and amphibole and discussed further in the results). We repeated calculations using different initial water content (2–4%) from temperatures slightly above the liquidus and then at 50 C steps.

RESULTS

Sampling sites and rock classification

From four intrusions analyzed in this study, two were emplaced in NZ mylonites (Koźmice and Brodziszów; Fig. 1c1-c2) and two within the Sowie Mountain gneisses (Przedborowa, Kluczowa; Fig. 1c3-c4). The Przedborowa and Kluczowa intrusions are composed of rocks with amphibole as the main mafic phase, whereas mafic minerals in the Koźmice and Brodziszów intrusions are clinopyroxene and biotite (Table SM2.2). Based on modal proportions of felsic phases (using the International Union of Geological Sciences (IUGS)-recommended Quartz-Alkali Feldspar-Plagioclase diagram of Streckeisen, 1976) Amp-bearing rocks can be classified as quartz monzodiorites and Cpx-bearing rocks as diorites to quartz diorites (Fig. 2a). However, based on the classification diagram of Debon & Le Fort (1983), the Amp-bearing rocks plot as monzodiorites to quartz monzodiorites and quartz monzonites, whereas Cpx-bearing rocks plot as monzodiorites to quartz monzonites (Fig. 2b). According to the chemical classification based on the Linear Discriminant Analysis (Bonin *et al.*, 2020), the studied rocks are magnesian, metaluminous, and calc-alkalic, sodic to alkali-calcic, potassic. Clearly, the rocks are difficult to classify as they represent several types of plutonic rocks, a feature typical for K-rich granitoids in post-orogenic settings (Bonin *et al.*, 2020). Therefore, for simplicity in this paper, the rocks are referred to as **amphibole monzodiorite** (AmpMzd) and **clinopyroxene monzodiorite** (CpxMzd).

Field relations and petrography

Amphibole monzodiorite is predominately medium-grained to fine-grained or porphyritic and contains varying proportions of mafic to felsic phases (Fig. 3a,b,c; Table SM 2.2). Rocks dominated by felsic phases also occur as veins or zones surrounding more mafic bodies (Fig. 3b,c,d). The contacts between the rock types are rarely observed but where visible are complex, e.g. porphyritic AmpMzd may form dismembered small bodies surrounded by more felsic compositions and by medium-grained AmpMzd (Fig. 3b). The AmpMzd is cut by pegmatitic veins and in places, irregular pegmatitic segregations are also observed (Fig. 3c,d). Rare enclaves of coarser-grained hornblendites (Fig. 3e) are observed in dioritic rocks or complex brecciated, pegmatitic zones (Fig. 3d). Based on these textural observations we conclude that the AmpMzd rocks have all the characteristics attributed usually to **appinites** (Murphy, 2020). This conclusion is consistent with the high abundance of euhedral amphibole in all samples including pegmatites (Fig. 3h). Relicts of clinopyroxene occur in amphibole cores in some samples. Accessories are magnetite (Ti-magnetite/hematite), sulfides, titanite, apatite and zircon. Small grains of ilmenite, allanite and uranian thorite were also detected.

Clinopyroxene monzodiorite is fine-grained in Koźmice and porphyritic in Brodziszów. The monzodioritic rock in Koźmice was termed vaugnerite previously (Puziewicz, 1988). Pegmatitic nests and breccias occur in both intrusions but are not as common as in AmpMzd and, generally, the monzodioritic rocks seem homogeneous at the outcrop scale (Fig. 3f). CpxMzd in both intrusions are dominated by plagioclase, biotite and clinopyroxene, clots of mafic crystals (Cpx, Amp, Bt) occur in Brodziszów. The Brodziszów intrusion contains abundant amphibole but, based on its chemical composition (see below), we consider it to be late to post-magmatic in origin. CpxMzd also contains K-feldspar, quartz and accessory apatite, sulfides, titanite, ilmenite and zircon.

Whole-rock composition

All the analyzed rocks belong to high-K (AmpMzd) and shoshonitic (AmpMzd, CpxMzd) suites (Fig. 4a, Peccerillo & Taylor, 1976). The samples with higher Si and K contents have higher modal abundances of K-feldspar and biotite. For all the analyzed samples, the SiO_2 content varies from 51 to 59 wt% and the range is similar for both AmpMzd and CpxMzd (Table SM2.2). As some chemical and petrological observations are distinct between rocks

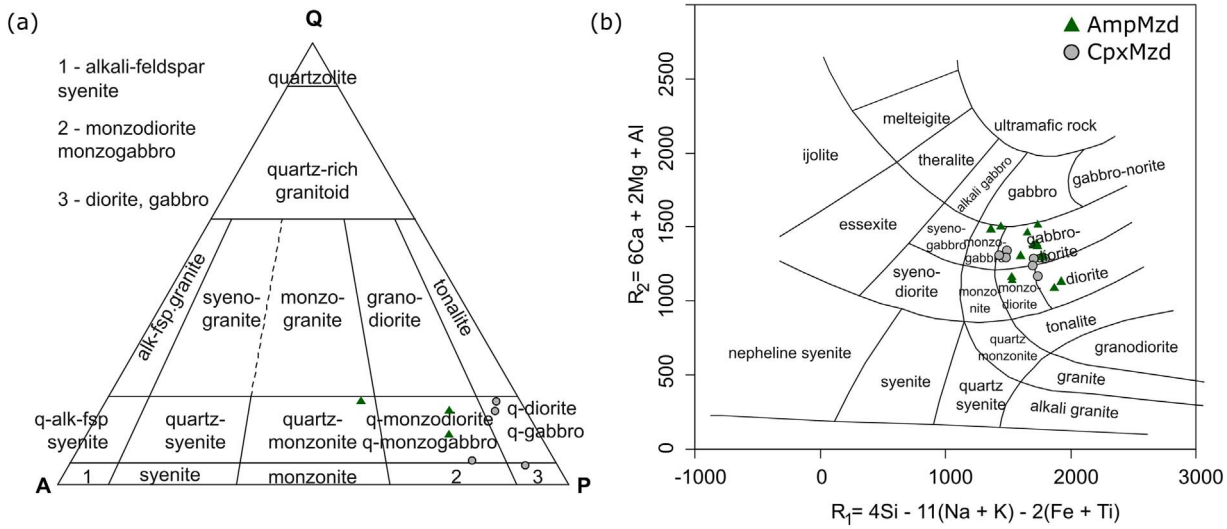

Figure 2. Classification of the studied rocks in (a) the IUGS-recommended QAP diagram of Streckeisen (1976) and (b) the R1-R2 classification diagram (De La Roche *et al.*, 1980).

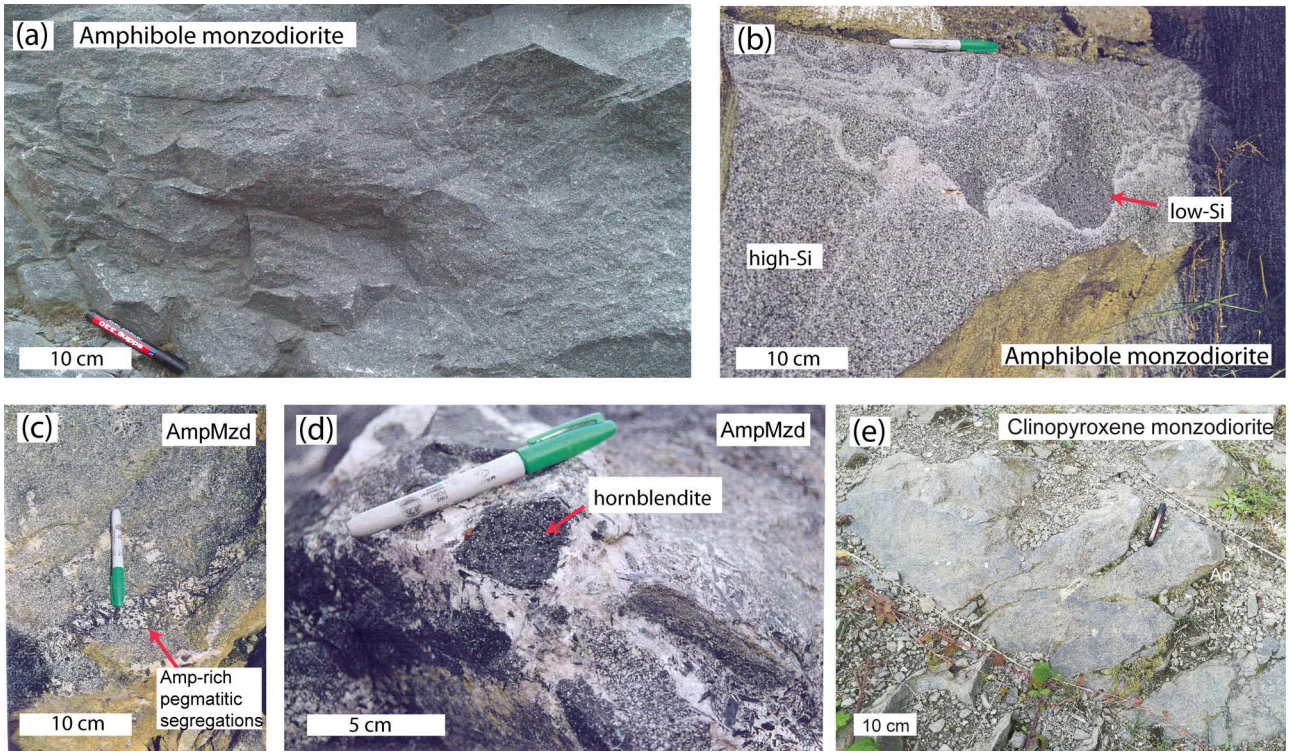

Figure 3. Field occurrences and petrography of amphibole and clinopyroxene monzodiorites (a) AmpMzd–Przedborowa, homogenous monzodiorite; (b) AmpMzd–Przedborowa, different types of monzodiorites with complex contacts within a single block; (c) AmpMzd–Przedborowa, pegmatitic segregations; (d) AmpMzd–Przedborowa, plutonic breccia composed of hornblendites and dioritic fragments enclosed in pegmatite; (e) CpxMzd–Koźmice, a representative CpxMzd in the outcrop.

with different silica content, the rocks are divided into low-Si ($SiO_2 \leq 55$ wt%) and high-Si ($SiO_2 > 55$ wt%) varieties (Fig. 4b). The distribution of REE, Ba, and Zr concentrations between AmpMzd and CpxMzd are similar (Fig. 4f,g,i–k). The differences between individual intrusions and samples include the following: (1) lower Sr (Fig. 4d), and higher Rb (Fig. 4e) contents in CpxMzd compared with AmpMzd; (2) the highest MgO, Ni and Cr concentrations in high-Si CpxMzd from Koźmice, in particular, Ni and Cr are at least three times higher than in all other samples (Fig. 4c for Cr, TableSM2.2); and (3) higher Sr contents in one sample (BN004C) consistent with the accumulation of plagioclase (Fig. 4b). The hornblendite sample analyzed from Kluczowa has high Mg, Cr and Ni and low contents of other trace elements (Fig. 4).

Based on the observed textural varieties and geochemical trends, we have selected six samples (three AmpMzd, three CpxMzd; Table SM2.1) for more detailed microchemical and isotopic studies.

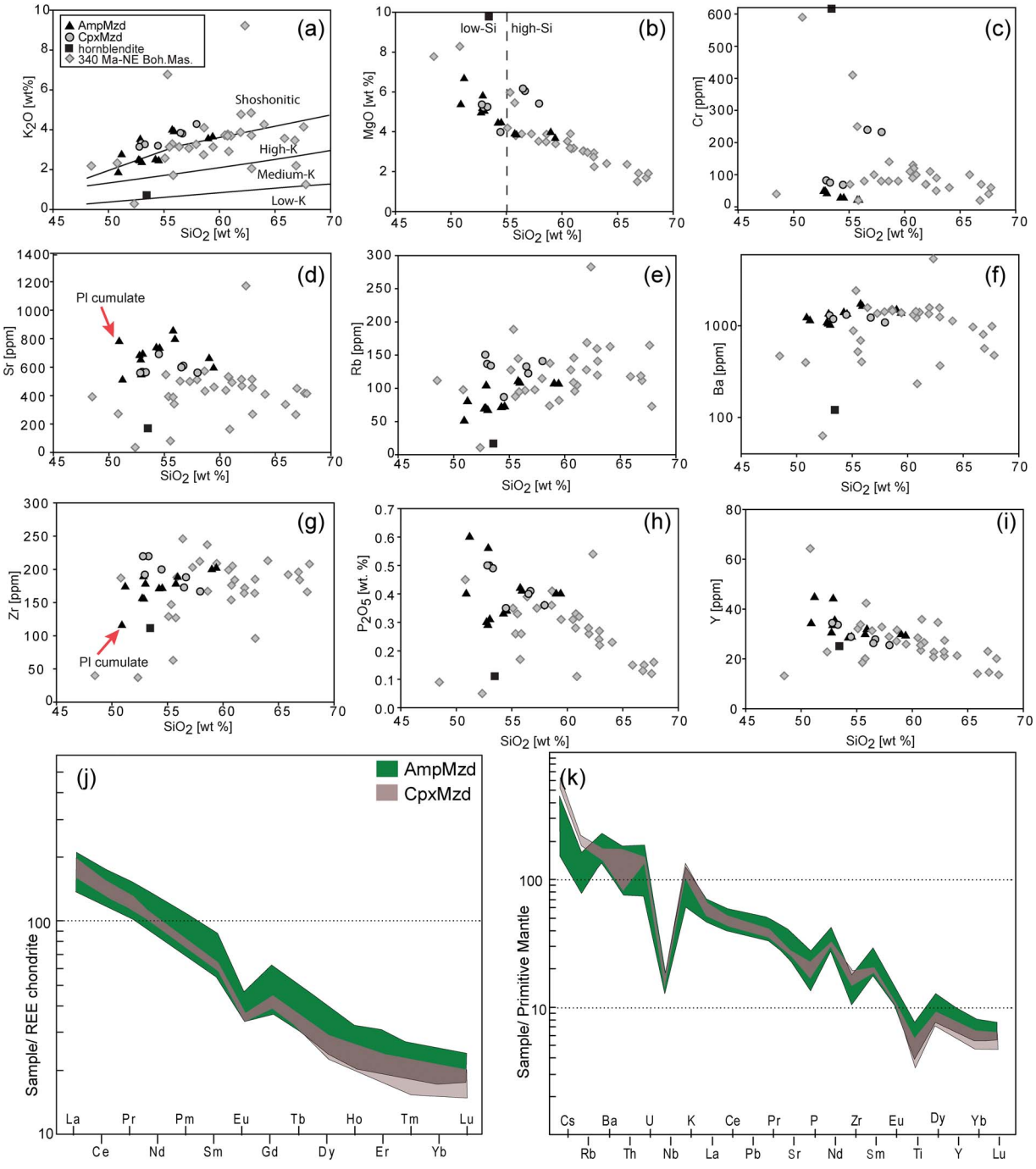

Figure 4. Chemical composition of the studied rocks compiled with data from Pietranik *et al.* (2013) compared with data from other occurrences of ca. 340 Ma igneous rocks in NE Bohemian Massif. Data sources: Staré Město, Jawornik and Kłodzko-Złoty Stok granitoids and associated mafic and ultramafic rocks (Jastrzębski *et al.*, 2018; Białek, 2020), Odra and Niemcza granitoids (Oberc-Dziedzic *et al.*, 2015). The classification in low-Si and high-Si rocks is shown in (b) and compositions interpreted as cumulates of plagioclase are indicated by arrows in (d) and (g).

Major minerals: occurrence and composition

Amphibole

In CpxMzd, amphibole is scarce and mostly forms rims around or replaces clinopyroxene (Fig. 5a,b,c). In AmpMzd amphibole is abundant and forms subhedral to euhedral grains (Fig. 5d) or clots of several grains with ragged rims (Fig. 5f). Ultramafic rocks are composed predominately of amphibole and minor biotite (Fig. 5e). Apatite occurs in hornblendites from Przedborowa, but not from Kluczowa. All amphiboles from AmpMzd (Przedborowa) are magmatic, whereas some from CpxMzd and AmpMzd in Kluczowa are magmatic, but others are secondary (Fig. 6a). Figure 6 shows that despite Kluczowa being classified as AmpMzd, the composition of the amphibole overlaps with that of CpxMzd and, therefore, only Przedborowa is considered as AmpMzd in this study.

Generally, amphiboles from AmpMzd are classified as pargasite, tschermakite and magnesio-hornblende, whereas those from CpxMzd are magnesio-hornblende

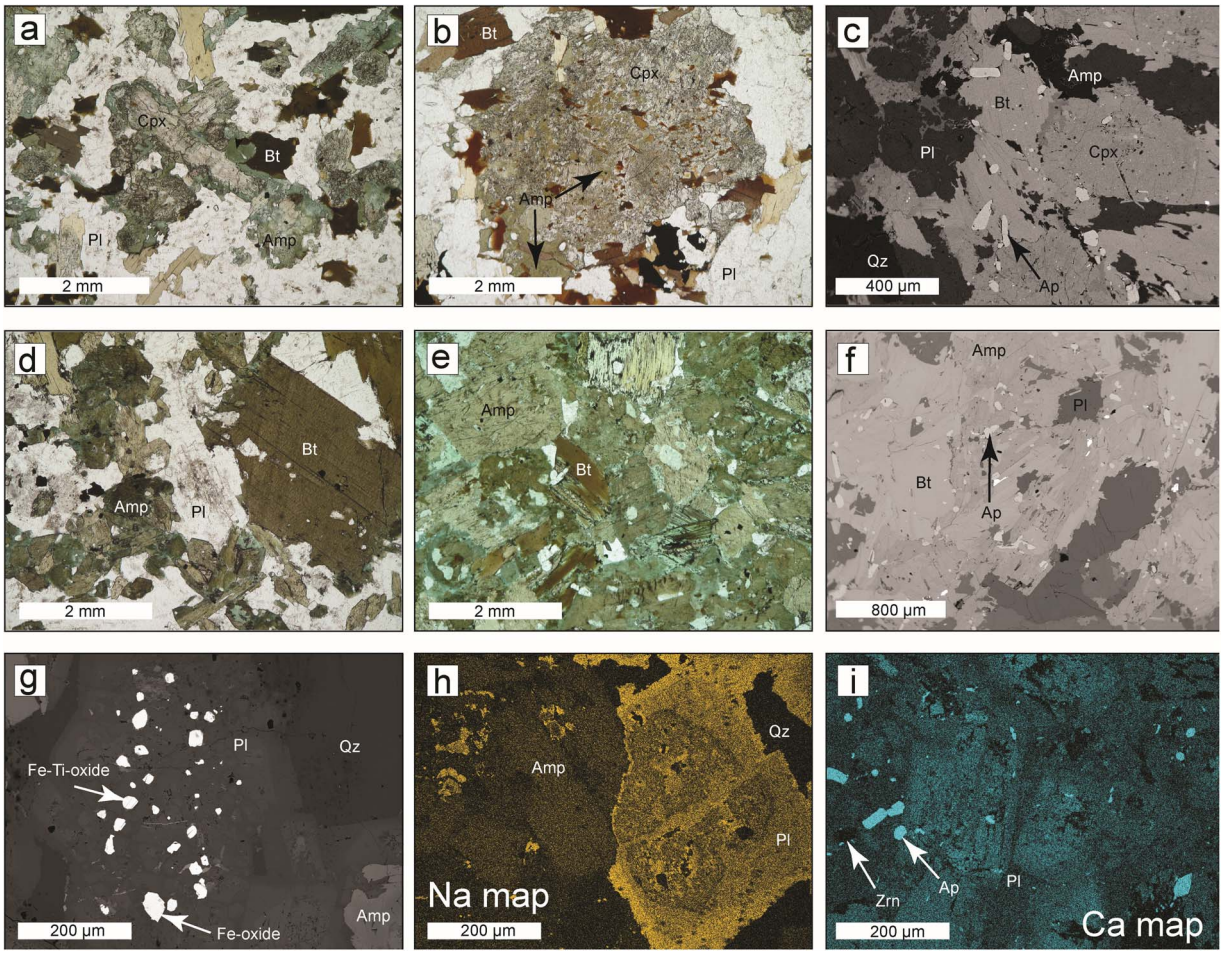

Figure 5. Petrography of the studied monzodiorites (a) clinopyroxene overgrown by late amphibole (high-Si CpxMzd, Koźmice), microscope view PPL; (b) clinopyroxene replaced by patches of secondary amphibole (low-Si CpxMzd, Brodziszów), microscope view PPL; (c) BSE image of typical CpxMzd structure (high-Si CpxMzd, Koźmice); (d) porphyritic AmpMzd with clots of euhedral amphibole (low-Si AmpMzd, Przedborowa), microscope view PPL; (e) amphibole-dominated ultramafic fragment enclosed in AmpMzd (Przedborowa), microscope view PPL; (f) BSE image of amphibole clot with ragged rims (AmpMzd, Kluczowa); (g) BSE image of plagioclase clot enclosing Fe-oxides (low-Si AmpMzd, Przedborowa); (h) EDS map of complex plagioclase, the intensity of the color is related to the concentration of Na (low-Si AmpMzd, Przedborowa); (i) EDS map of a plagioclase clot, the intensity of the color is related to the concentration of Ca (low-Si AmpMzd, Przedborowa). The mineral symbols after Warr (2021).

and actinolite/tremolite (Hawthorne *et al.*, 2012; Fig. 6d; the classification of Leake *et al.*, 1997 is shown for comparison; Table SM 2.3 shows detailed data and amphibole classification). Amphibole from low-Si AmpMzd has the highest TiO_2, K_2O, Al^{TOT}, Al^{IV} and $(Na+K)_A$ a. p.f.u. (Fig 6 a,b,c). Grains are zoned toward lower Al^{TOT} and Al^{IV}, Ti, Na, a.p.f.u in the rims. Also, some amphibole from low-Si AmpMzd plots in the alkaline field in TiO_2 versus K_2O diagram (Fig. 6b).

The temperature of amphibole crystallization was estimated by the geothermometer of Putirka (2016). The temperatures are 830–950°C for low-Si AmpMzd, 750–900°C for high-Si AmpMzd and 650–800°C for low and high-Si CpxMzd (Table SM 2.3). The small set of analyses from a single thin section for Kluczowa AmpMzd yielded temperatures similar to those for CpxMzd (Table SM 2.3). Pressure estimates are more problematic as they require equilibrium between amphibole and the liquid, and the studied amphiboles are not in equilibrium with their whole-rock compositions for both Fe-Mg exchange and SiO_2. Such equilibrium should be expected for AmpMzd, where amphibole is an early crystallizing phase. However, the lowest K_D(Fe-Mg) calculated from amphibole composition in AmpMzd is 0.47 (Eq. 2 of Putirka, 2016) and corresponds to the lowest predicted $SiO_2 = 60$ wt%, therefore 9 wt% higher than the whole-rock composition (Eq. 10 of Putirka, 2016). The lowest predicted SiO_2 for high-Si AmpMzd is also higher by more than 10 wt% than the whole rock—66 wt%. Pressure estimates based on the amphibole-only barometer of Mutch *et al.* (2016) calculated for amphibole rims in presumed textural equilibrium with plagioclase (An15–80) + biotite + quartz + alkali feldspar + ilmenite/titanite + magnetite + apatite are 5 kbar for low-Si AmpMzd and 3 kbar for all other rock types including high-Si AmpMzd (Table SM 2.3). Oxygen fugacity estimates based on the hornblende oxybarometer calibrations of Ridolfi *et al.* (2010) yield fO_2 between FMQ + 0.9 and NNO + 4.6 with the highest fO_2 estimated for amphibole from low-Si AmpMzd and the lowest for high-Si AmpMzd and low-Si CpxMzd (Table SM 2.3).

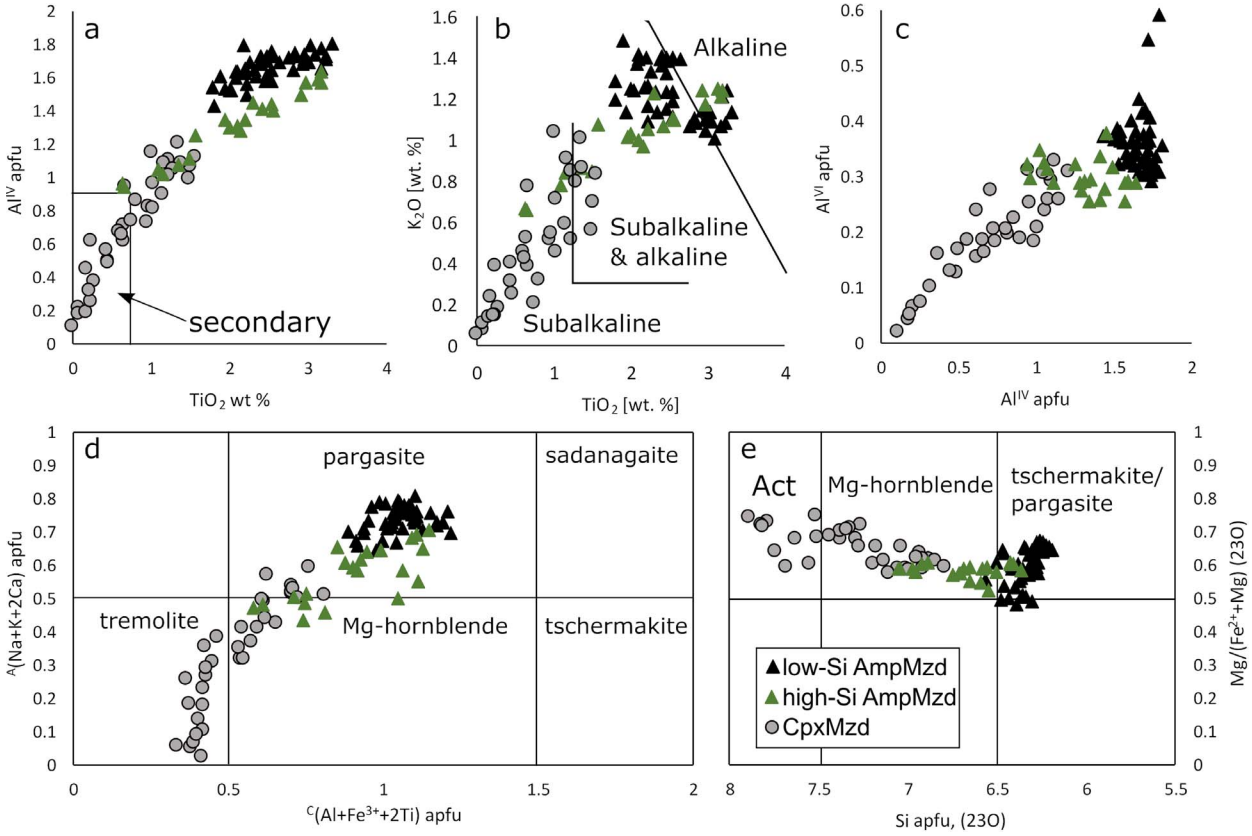

Figure 6. Amphibole composition: (a) The diagram based on Molina *et al.* (2009) and Cambeses *et al.* (2021), showing that Amp from CpxMzd is partly of magmatic and partly of secondary origin; (b) the diagram proposed by Molina *et al.* (2009) showing crystallization of amphiboles from chemically distinct melts, particularly for the group of analyses plotting in the alkaline field; (c) AlIV versus AlVI calculated after Putirka (2016); (d) classification of calcic amphiboles after Hawthorne *et al.* (2012); (e) classification of amphiboles after Leake *et al.* (1997). Since AmpMzd amphiboles from Przedborowa have (Na + K)A both above and below 0.5 (Table SM2.3) two names are shown, pargasite for (Na + K)A > 0.5 and tschermakite for (Na + K)A < 0.5. Black triangles, amphibole from low-Si AmpMzd, Przedborowa intrusion; dark green triangles, amphibole from high-Si AmpMzd, Przedborowa intrusion; light green triangles, amphibole from AmpMzd, Kluczowa intrusion; gray circles, CpxMzd, undifferentiated.

Plagioclase

Plagioclase is normally zoned with a range (An_{60} to An_{30}) of analyzed anorthite contents in high-Si AmpMzd and CpxMzd (Fig. 7a). Low-Si AmpMzd contains rounded plagioclase cores (An_{79} to An_{65}) surrounded by two euhedral zones with lower An content (An_{51} to An_{18}, Fig. 5h). Notably, the change in An content in AmpMzd is step-like with the characteristic absence of An values for specific ranges (Fig. 7a). Plagioclase in high-Si AmpMzd and CpxMzd is evenly distributed, whereas it commonly occurs as clots in low-Si AmpMzd (Fig. 5g,h,i). The clots may enclose either Fe-oxides (Fig. 5g), abundant apatite or, more rarely, zircon (Fig. 5i). Such clots are composed of separate high-An cores surrounded by low-An plagioclase (Fig. 5g,i).

Strontium content in plagioclase is higher in AmpDrt (average 2850 ppm) than in CpxDrt (average 1870 ppm). When Sr content in plagioclase is re-calculated to equilibrium Sr-in-melt composition, a mismatch between plagioclase from low-Si AmpMzd and whole-rock occurs (Fig. 7b).

Biotite and pyroxene

Biotite composition is similar in AmpMzd and CpxMzd (Table SM2.5). The major difference between both rock types is the Al content, which is higher in biotite from AmpMzd from Przedborowa and Cl content and higher in biotite from CpxMzd. Clinopyroxene was analyzed only in CpxMzd (Table SM2.6) and is classified as diopside (Morimoto, 1988). Pressure estimates for clinopyroxenes are 0.7–4.8 kbar (Neave & Putirka, 2017; Table SM2.6), which is consistent with pressures indicated by the Al-in-amphibole barometer for AmpMzd and CpxMzd.

Zircon occurrence and composition

All zircon grains show oscillatory zonation characteristics for magmatic zircon (Fig. 8a,b; Supplementary Material SM3). A subset of zircon grains from AmpMzd exhibits dark CL rims with porous structure (Table SM2.7). Generally, zircon from low-Si AmpMzd is coarser-grained and more elongate than zircon from other diorite types. In CpxMzd, zircon is euhedral and forms inclusions in the outer parts of plagioclase or clinopyroxene (Fig. 8c). In AmpMzd, zircon is euhedral to subhedral and is usually surrounded by quartz, K-feldspar and/or biotite (Fig. 8d), but occurs also within low-An plagioclase (Fig. 5i). These textures suggest that zircon was a late phase crystallizing after plagioclase and amphibole in AmpMzd, and relatively late in CpxMzd, crystallizing contemporaneously with plagioclase rims

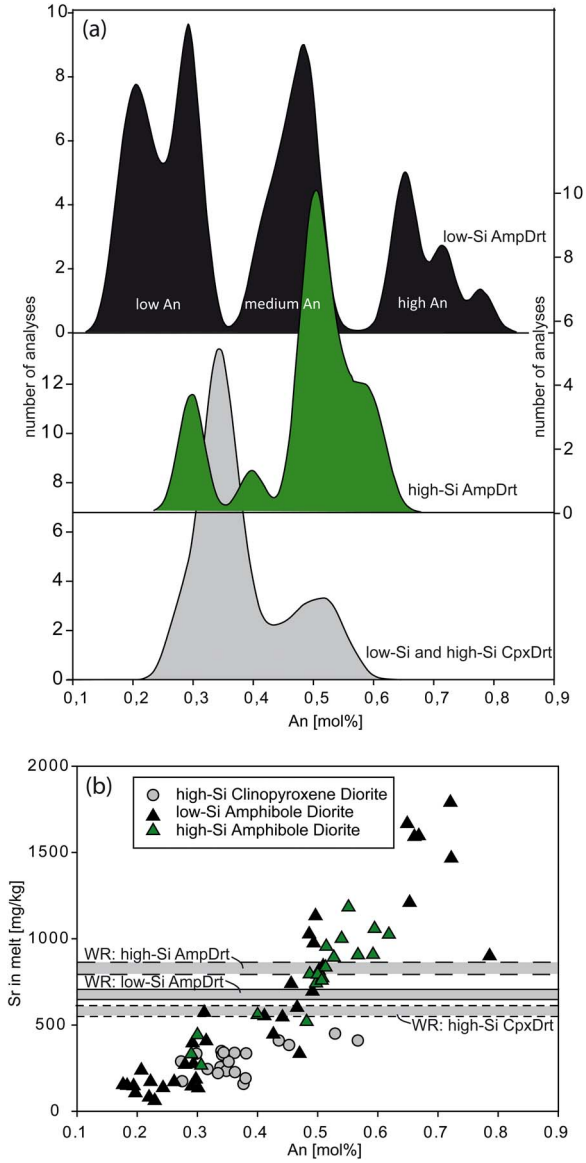

Figure 7. Plagioclase composition: (a) Relative distribution of An content in plagioclase in the studied rocks; and (b) Sr-in-the-melt calculated for the set of microprobe analyses using partition coefficients of Bindeman *et al.* (1998) for analysed An content. The range of Sr contents in whole rocks is shown as bands. Discrepancies between a whole rock and plagioclase composition are addressed in the text.

(Fig. 8e,f). Microprobe analyses show that, generally, Hf increases rimwards in zircon in both CpxMzd and AmpMzd (Fig. 8a,b), but the pattern for Y is more complex, with recurring higher and lower Y contents during crystallization (Table SM2.7).

Age determinations

Nine grains were dated from each low-Si AmpMzd and high-Si CpxMzd using the CA-ID-TIMS method. The samples were chosen from the same rock types dated by Pietranik *et al.* (2013). Three grains from each of the samples analyzed show significantly younger ages than the mean for the remaining analyses, which are attributed to small degrees of residual Pb loss after chemical abrasion as suggested in other cases (e.g. Davies *et al.*, 2021). These grains are not considered any further. Six grains from CpxMzd yield ^{206}Pb-^{238}U ages that are identical within error, giving a weighted mean age of 340.37 ± 0.24 Ma (MSWD = 1.5). Six grains from AmpMzd yield a weighted mean age of 340.02 ± 0.16 Ma (MSWD = 0.63). (Fig. 9, Table SM2.8).

Zircon composition: trace elements

Zircon from AmpMzd and CpxMzd show distinct Eu anomalies ($Eu/Eu^* = Eu_N/\sqrt{(Sm_N * FGd_N)}$), Ti, Hf, Eu, U contents and Yb/Dy ratios (Table SM2.10). In particular, zircon from AmpMzd has higher Eu/Eu*, Th/U and Yb/Dy ratios (Fig. 10a,f,g), but lower Ti, Ta, and Hf concentrations (Fig. 10d,e) and U/Yb ratios (Fig. 10b) than those from CpxMzd. The most remarkable discriminator between the two rock types is zircon Eu/Eu*, especially considering that this parameter shows only limited variations in the whole-rock compositions. The Eu/Eu* in zircon varies also between low- and high-Si rock types in both AmpMzd and CpxMzd and is always higher in high-Si samples (Fig. 10a).

The differences in Ti content in zircon suggest differences in crystallization temperatures, as calculated using a Ti-in-zircon thermometer. However, as the rocks do not contain rutile and quartz is late, the calculations require a_{TiO2} and a_{SiO2} to be estimated (Watson *et al.*, 2006; Schiller & Finger, 2019). The studied rocks contain the same assemblage of Ti phases titanite and ilmenite/Ti-magnetite, which suggests comparable a_{TiO2} for both CpxMzd and AmpMzd. Based on MELTS modeling (Ghiorso & Sack, 1995) that calculates the affinity of quartz and rutile at different stages of crystallization (approach presented by Schiller & Finger, 2019), both rock types yield similar a_{TiO2} of 0.20–0.30 at 1000°C increasing to 0.30–0.50 at 800°C (Table SM2.9). Using the same modeling approach, a_{SiO2} increases over the same temperature interval from 0.60 to 0.80. Therefore, we use the same activities for all studied samples ($a_{SiO2} = 0.8$ and $a_{TiO2} = 0.40$) to calculate Ti-in-zircon temperatures. For these activity values, the temperatures are higher for CpxMzd (860 ± 51°C for low-Si and 884 ± 54°C for high-Si types) than for AmpMzd (780 ± 27°C for low-Si and 793 ± 29°C for high-Si types, Table SM2.10). Choosing different activity values changes absolute temperatures (not exceeding 100°C), but the relative differences remain. These differences are not reflected by zircon saturation temperatures that are very similar for CpxMzd and AmpMzd at 590–660°C (Boehnke *et al.*, 2013) or 640–700°C (Watson & Harrison, 1983).

The oxygen fugacity in the melt that precipitated zircon was estimated using the oxybarometer of Loucks *et al.* (2020). The higher fO_2 are predicted for zircon from AmpMzd with overlapping values for low-Si and high-Si samples from FMQ = 0.2 to FMQ = 1.5, the values for low-Si and high-Si CpxMzd are also overlapping and range from FMQ = − 0.5 to FMQ = 0.7 with few lower values observed in CpxMzd (Table SM2.10).

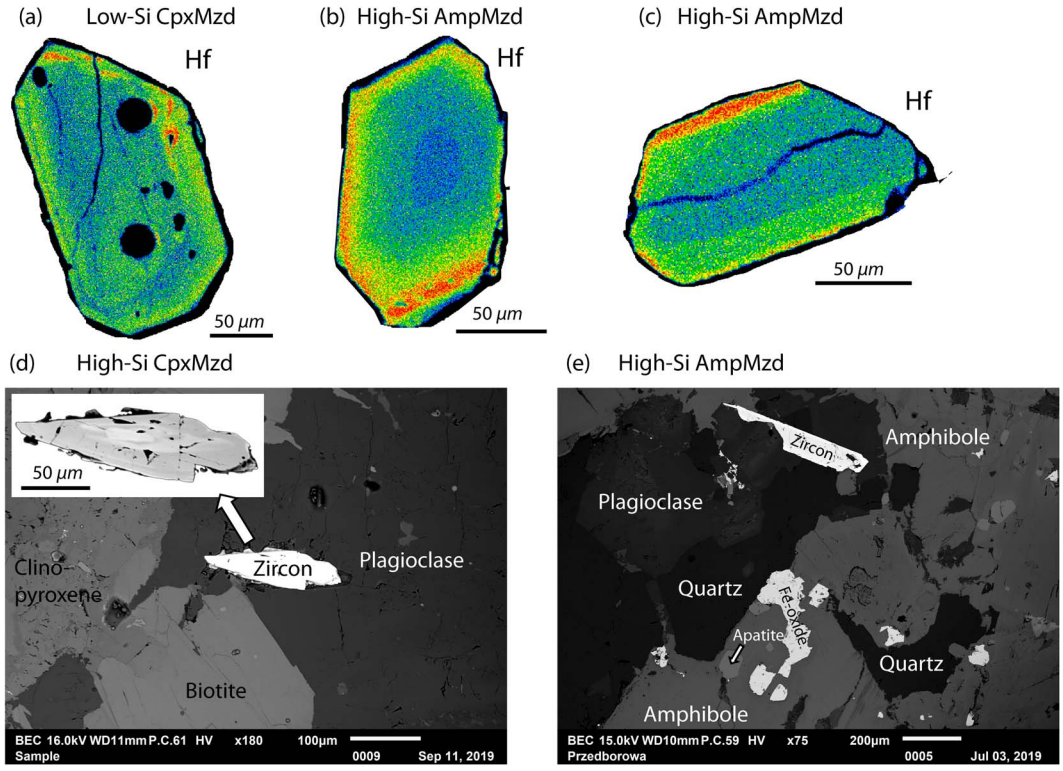

Figure 8. (a–c) Hafnium compositional zoning in zircon indicated by electron microprobe mapping (blue shows the minimum and red maximum content); and (d,e) back-scattered images showing the structural position of zircon. Mineral symbols after Warr (2021).

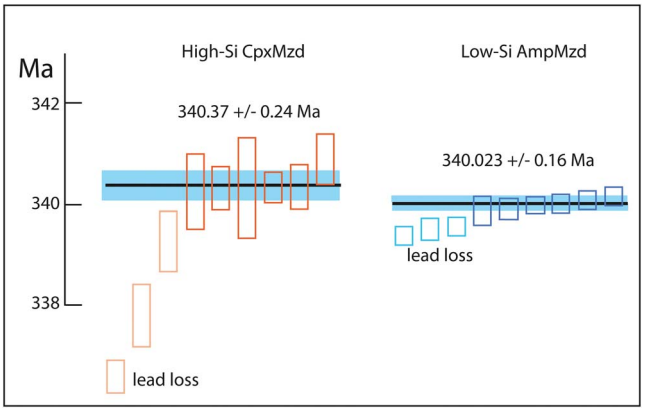

Figure 9. Zircon CA-ID-TIMS ages presented as weighted mean 206Pb/238 U ages with 2σ uncertainty bars for individual analyses and 2SE for the pooled age. (a) Amphibole monzodiorite and (b) Clinopyroxene monzodiorite.

Zircon composition: Hf isotopes

The variation in Hf isotopic composition is generally negligible within a sample or rock type, but different between rock types (Fig. 11; Table SM2.11). The most radiogenic εHf occurs in high-Si CpxMzd ($\varepsilon Hf = -1.8 \pm 0.4$; $n = 12$); less radiogenic εHf occurs in both low-Si types ($\varepsilon Hf = -3.5 \pm 0.8$; n = 10 for CpxMzd and $\varepsilon Hf = -3.3 \pm 0.5$; $n = 24$ for AmpMzd) and the least radiogenic in high-Si AmpMzd samples ($\varepsilon Hf = -4.7 \pm 0.5$; $n = 22$). Additional zircon analyses included granodiorite from Kozmice (CpxMzd and the granodiorite have sharp contact), which yielded $\varepsilon Hf = -4.3 \pm 1.3$ ($n = 10$). For comparison, the range of εNd analyzed for 340 Ma igneous rocks in the NE Bohemian Massif (Oberc-Dziedzic *et al.*, 2015; Jastrzębski *et al.*, 2018) was recalculated to εHf values using the equation for 'terrestrial array' [$\varepsilon Hf = (1.55 \times \varepsilon Nd) + 1.21$] by Vervoort *et al.* (2011) and yielded εHf in the range from −7 to −1.5. The εHf values generally agree between this and the previous studies (Fig. 11f).

Zircon composition: O isotopes

Oxygen isotopes in zircon are from +4.4‰ to +10.8‰ (Fig. 11, Table SM2.12). The zircon from high-Si types (both AmpMzd and CpxMzd) has variable isotope composition with $\delta^{18}O$ often exceeding 8‰, although low values (<6‰) occur (Fig. 11a,c). On the other hand, O isotopes are more homogeneous in low-Si rocks with values exceeding 8‰ observed only in a few grains (Fig. 11a,c). The $\delta^{18}O$ values are similar to those measured in other 340 Ma rocks from the NE Bohemian Massif (Fig. 11e).

Other accessory minerals

Apatite is a common and abundant mineral in all rocks. It is enclosed mainly by mafic phases (Amp + Bt in AmpMzd and Cpx and Bt in CpxMzd; Table SM2.13), but it occurs also in low-An plagioclase in AmpMzd and hornblendite from Przedborowa (Fig. 5e,i). The saturation temperatures are 810–850°C in low-Si AmpMzd, 905°C in high-Si AmpMzd, 890°C in low-Si CpxMzd and 915°C in high-Si CpxMzd (Harrison & Watson, 1984). Apatite compositions were measured by electron microprobe and

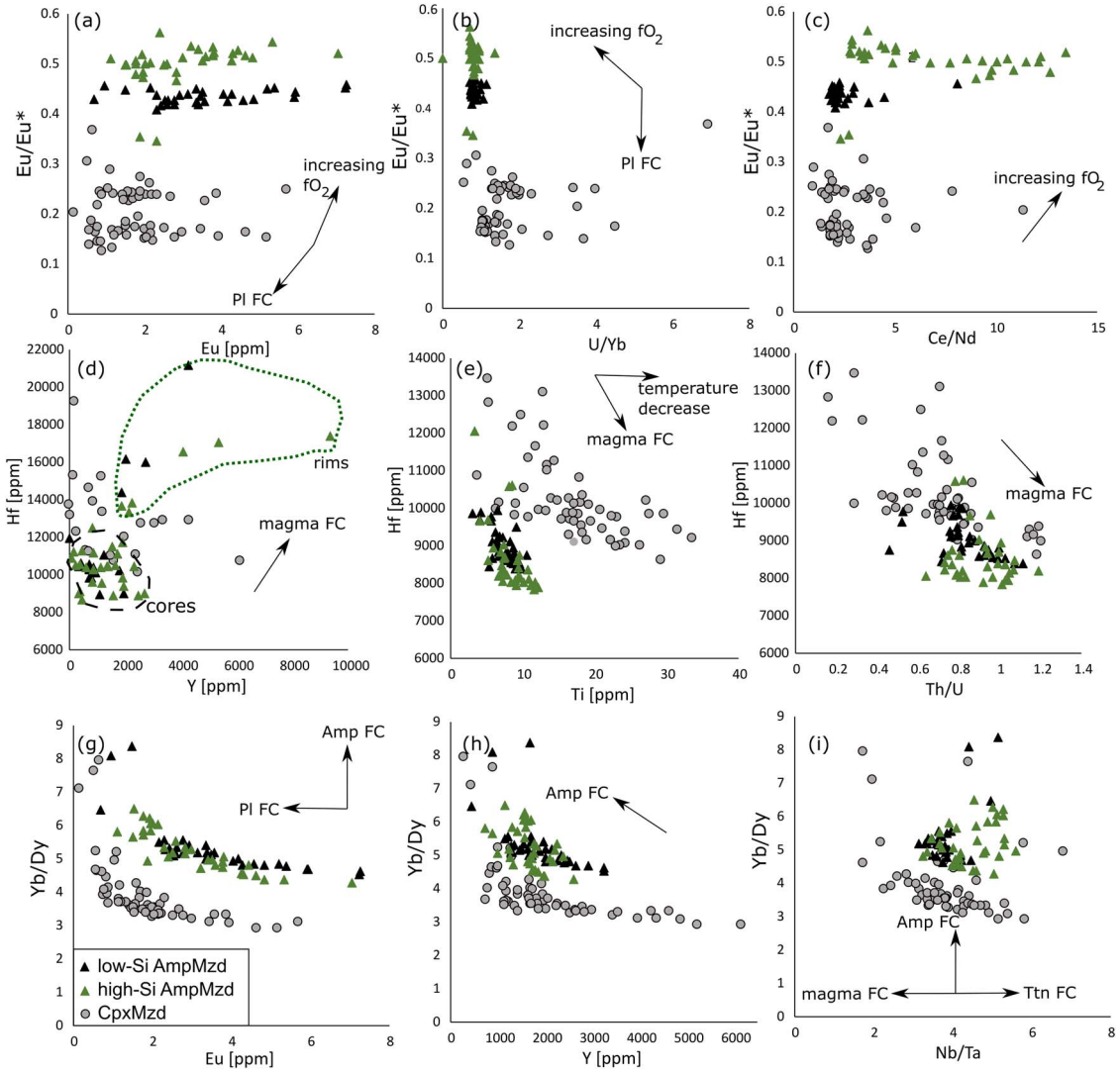

Figure 10. Trace element in zircon, Eu/Eu* = EuN/$\sqrt{}$(SmN*GdN) with the concentrations normalized to chondrite values of Anders & Grevesse (1989). Vectors indicate an implied change of zircon composition with distinct processes of magma differentiation (Amp FC, amphibole fractionation; Pl FC, plagioclase fractionation). The slopes, lengths and directions of vectors are only approximate to define qualitatively the presumed dominating factor controlling the change in zircon composition. The plots present LA-ICP-MS data except for (d), which presents electron microprobe data with the possibility to delineate cores and rims composition.

the element showing variability between the studied rock types is Y (Fig. 12a). Generally, apatite from AmpMzd is characterized by low Y (mostly below the detection limit), whereas apatite from CpxDrt has high Y.

Titanite is scarce and forms small, subhedral to anhedral grains in biotite of magmatic origin or flakes surrounding Fe-oxides or filling cleavage zones in biotite, where it is most probably of secondary origin. Titanite is compositionally similar between the studied rocks.

Opaque minerals are euhedral Fe-sulfides in CpxMzd and predominately Fe- and Fe-Ti-oxides in AmpMzd. Iron sulfides occur also in AmpMzd but are always rounded and enclosed in amphibole or Fe-oxides. Iron oxides are accompanied by Cu-Fe sulfides and minuscule (Pb, Ag, Se, Cu)-metallic phases. A specific assemblage of Fe-oxide with abundant apatite occurs only in AmpMzd. Altogether the rounded Fe-sulfides and late crystallization of domains rich in Fe-oxide and apatite resemble textures formed in experiments, where immiscible liquids were present (Hou *et al.*, 2018).

DISCUSSION

A short-lived magmatic episode at 340 Ma

Magmatic activity in collisional orogens is usually episodic with different magma batches emplaced at different stages of the orogenic evolution (Walker *et al.*, 2015; Schaltegger *et al.*, 2019; Trubač *et al.*, 2020). In terms of magma differentiation, magmatism in collisional zones is much more complex than in arcs as the diversity of potential magma sources increases (Dias *et al.*, 2002; Cambeses *et al.*, 2019; Trubač *et al.*, 2020), and repeated extensional episodes may further complicate the record through phases of exhumation and decompressional melting (Collins *et al.*, 2020a). Six episodes of magmatism were detected in the Bohemian

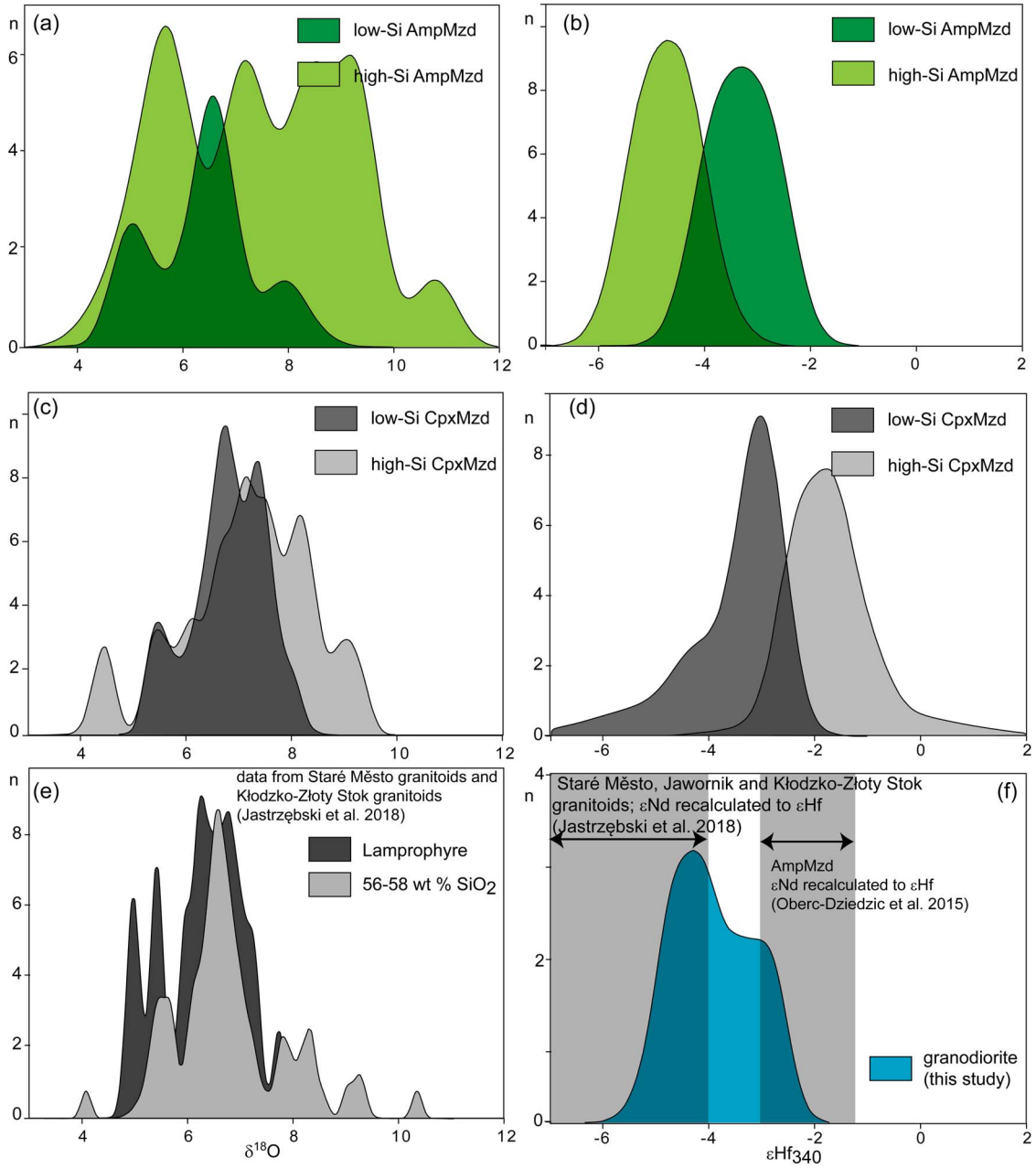

Figure 11. Zircon Hf (right) and O (left) isotope compositions presented as relative probability curves. The δ18O data from the studied diorites were compared with δ18O data in zircon from 340 Ma magmatism in the NE Bohemian Massif including Staré Město and Kłodzko–Złoty Stok granitoids (Jastrzębski *et al.*, 2018). εHf data were compared with εNd data from 340 Ma Staré Město, Jawornik, Kłodzko–Złoty Stok and Przedborowa AmpMzd intrusions (Oberc-Dziedzic *et al.*, 2015; Jastrzębski *et al.*, 2018) by recalculating to εHf using terrestrial array equation (Vervoort *et al.*, 2011).

Massif from 375 to 296 Ma. At ca. 340 Ma, a change from mantle-dominated to crustal-dominated magma sources likely recorded the switch from continental arc to post-collisional magmatism (Žák *et al.*, 2014; Trubač *et al.*, 2020) probably correlated with the subcontinental lithospheric mantle delamination (Gutiérrez-Alonso *et al.*, 2011; Dostal *et al.*, 2020). In detail, three magmatic episodes in the Bohemian Massif overlap with the 340 Ma age: syn-collisional arc magmatism (346.8–340.8 Ma), syn- to post-collisional (341.1–334.6 Ma) and ultrapotassic magmatism (350–336.6 Ma; Trubač *et al.*, 2020). The LA-ICP-MS zircon age obtained for the studied rocks in previous studies was distinct for wet and dry rocks (341.8 ± 1.9 Ma (2SD) for low-Si AmpMzd and 335.6 ± 2.3 Ma (2SD) for high-Si CpxMzd) supposedly consistent with a record of a changing geotectonic setting (Pietranik *et al.*, 2013). However, this picture is no longer consistent with the results of the high-precision U–Pb zircon dating in the present study, which imply that the magmatism was more restricted in time. Since Ti-in-zircon temperatures are evenly scattered around the median temperature, the zircon population is very likely autocrystic and dates crystallization (Schiller & Finger, 2019). Also, zircon saturation temperatures lower than Ti-in-zircon temperatures reflect late zircon crystallization from the fractionated melt with the composition more

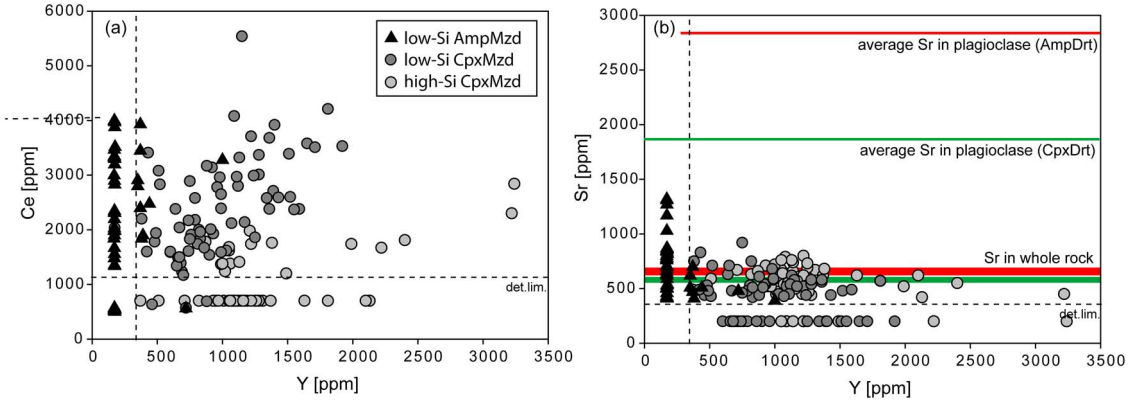

Figure 12. Apatite composition in the studied rocks. The analyses below the detection limits (indicated as dashed lines) are shown at $^1/_2$*det.lim. values in order to present the range of values for the second element.

evolved compared with the whole-rock composition, which has been used for calculations. Therefore, zircon ages indicate that monzodioritic magmas with distinct ferromagnesian rock-forming phases (clinopyroxene and amphibole) formed almost contemporaneously at 340 Ma in the same tectonic setting, probably belonging to the third episode of Trubač *et al.* (2020). This in turn implies the complexity of magma formation processes at the local scale with distinct sources contributing to each intrusion.

Diversity of crystallization conditions during 340 Ma magmatic episode

Crystallization experiments of basaltic to andesitic magmas that are close in composition to the studied rocks show that amphibole can be an early crystallizing phase for a range of pressures and oxygen fugacities when water contents in magma approach water saturation (Nandedkar *et al.*, 2014; Melekhova *et al.*, 2015, 2017; Ulmer *et al.*, 2018). The early crystallization of amphibole and the late crystallization of plagioclase drives the coexisting melt toward peraluminous composition (Alumina Saturation Index ASI > 1), which is not typical of arc magmas (Clemens *et al.*, 2021), but more common in collisional settings (e.g. Adamello, Ulmer *et al.*, 2018). High ASI magmas have a composition that is consistent with hydrous magma crystallization (Fig. 13a) but could be also due to the assimilation of clay-rich sediments (Clemens *et al.*, 2021). In terms of peraluminosity, the studied rocks plot within the compositional field typical for hydrous magmas for low-Si AmpMzd but high-Si AmpMzd straddle the boundary and high-Si CpxMzd plots within metaluminous trend, typical for the majority of arc magmas (Fig. 13a). The implication is that some of the studied rocks could have formed from magmas sufficiently enriched in water to suppress plagioclase crystallization, which is also consistent with the presence of hornblendites in AmpMzd. However, textural observations suggest that high-An plagioclase is an early phase in AmpMzd, as the rounded high-An cores are present in low-Si AmpMzd and euhedral plagioclase co-crystallizing with amphibole is common in high-Si AmpMzd. An independent record of the crystallization sequence comes from zircon that has distinct compositions in AmpMzd and CpxMzd. Many of the compositional differences may be attributed to the crystallization of amphibole or plagioclase prior to zircon. In detail, zircon from AmpMzd has higher Eu/Eu* and higher Eu/Dy_N contents (Fig. 14), a melt signature that suggests that plagioclase was a late crystallizing phase and that oxygen fugacity was low enough to stabilize enough Eu^{2+} in the melt to make it incompatible in the early crystallized amphibole (Nandedkar *et al.*, 2016). Also, the elemental ratios that increase during amphibole crystallization (e.g. Zr/Hf and Yb/Dy_N) due to differences in compatibility between the two elements (Klein *et al.*, 1997) are higher in zircon from AmpMzd (Fig. 14; Fig. SM2.7). However, the latter ratios cannot be used unambiguously as the record of solely amphibole fractionation, because clinopyroxene fractionation would have a similar effect on magma chemistry as these phases have similar partition coefficients at similar conditions (Ubide *et al.*, 2014; Iveson *et al.*, 2018). For the studied rocks, we suggest that the concentrations of amphibole/clinopyroxene-compatible elements are lower in zircon from AmpMzd than CpxMzd because AmpMzd was affected only by amphibole-dominated fractionation (wet magma), whereas CpxMzd by fractionation of both clinopyroxene and plagioclase (dry, dump magma). Using zircon as an additional indicator of hydrous magma crystallization conditions is important because (a) amphibole is not always present in hydrous magmas, e.g. magmas that contain only clinopyroxene phenocrysts could have evolved by amphibole fractionation (e.g. Melekhova *et al.*, 2015); (b) the modal composition may be misleading, because it may not represent the melt composition, but an accumulation of early crystallized phases; (c) zircon composition may further support magmatic versus late- to post-magmatic amphibole formation; and (d) evolution along the 'peraluminous trend' is not necessarily due to fractionation of hydrous magmas, but could indicate assimilation of Al-rich material (Clemens *et al.*, 2021). We suggest that combined records of delayed

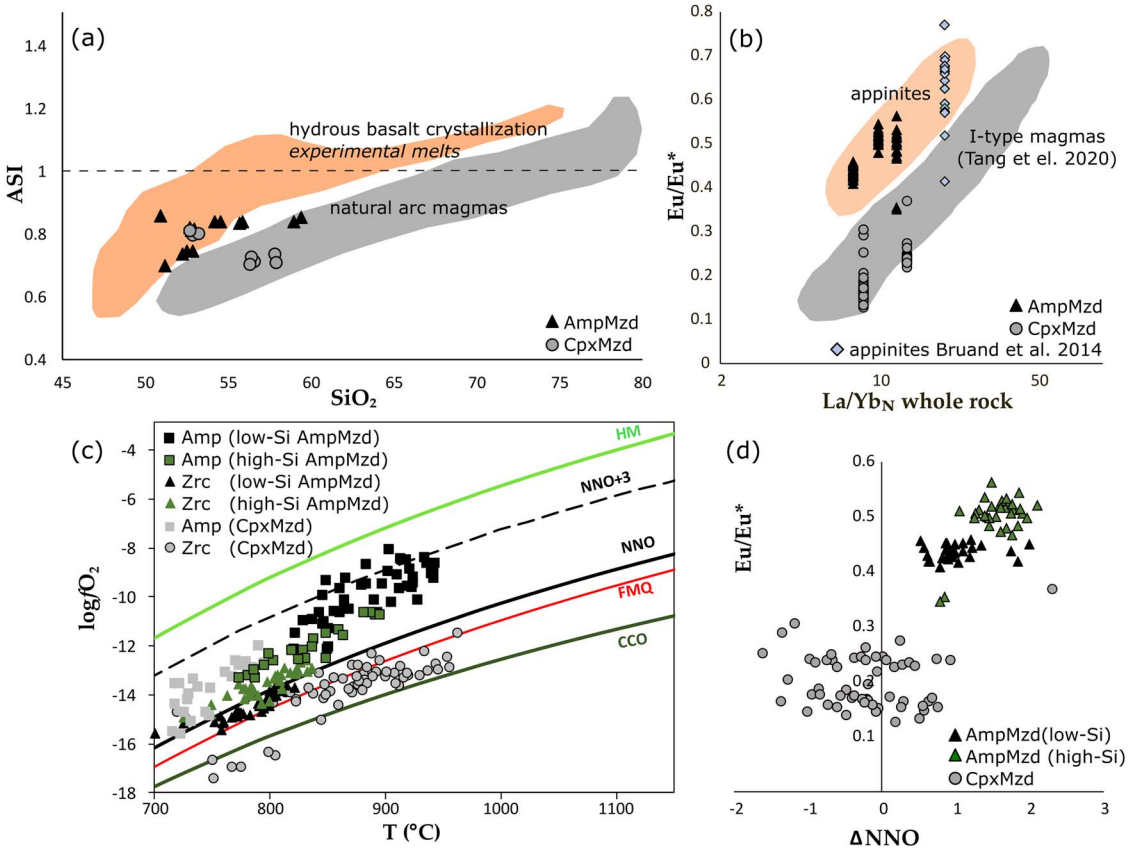

Figure 13. (a) Diagram showing whole-rock compositions of studied rocks plotted over fields of experimental hydrous melts (orange) and the compilation of typical arc magmas (gray), the fields are delineated based on the data presented in Clemens *et al.* (2021). (b) Normalized La/Yb ratio in whole rocks against Eu/Eu* in zircon (modified after Tang *et al.*, 2020), the gray field encompasses analyses presented by Tang *et al.* (2020), the orange field encompasses zircon analyses from AmpMzd from this study and appinite zircon from Bruand *et al.* (2014). (c) Oxygen fugacities calculated for amphibole and zircon using equations of Ridolfi and Renzulli (2012) and Loucks *et al.* (2020), respectively. (d) Correlation between Eu/Eu* and ΔFMQ calculated using the oxybarometer of Loucks *et al.* (2020) based on Ce-Ti-U concentrations.

plagioclase crystallization (elevated Eu/Eu* and Eu/Dy_N) and amphibole fractionation (high Zr/Hf, Hf, Yb/Dy) in zircon are consistent with the crystallization of hydrous magmas (Fig. 14a,b) and should provide additional information on the (a), (b), (c) and (d) scenarios above. Zircon analyses are particularly useful to detect wet magma crystallization in settings where a full appinite suite is absent. This is the case in the studied area, where only more mafic appinitic members are present, whereas felsic high Sr-Ba granites (common in Caledonides; Fowler *et al.*, 2008) do not occur.

Altogether, plagioclase is an important mineral controlling Eu/Eu* in zircon and may reflect the depth of the magma formation as the magmas formed within the garnet-stability field have higher Eu/Eu* in zircon and La/Yb in whole rock than the magmas formed at shallower depths in the plagioclase stability field (Tang *et al.*, 2020). The zircon from CpxMzd fits in the trend of Tang *et al.* (2020), whereas zircon from AmpMzd plots above the trend, similar to zircon from Scottish appinites (Bruand *et al.*, 2014). The zircons form a trend that runs parallel to that suggested by Tang *et al.* (2020), but at higher Eu/Eu^*_{zircon} for given La/Yb_{WR} (Fig. 13b). Our interpretation is that hydrous mafic to intermediate magmas such as appinites form in collisional settings at different crustal depths, but their hydrous nature can be, nevertheless, detected using Eu/Eu* in zircon. The abundance of such magmas is not clear, it seems that less hydrous magmas, characterized by the early plagioclase crystallization are more abundant, suggesting perhaps that fluid-free melting is a dominant process of silicic magma formation in this collisional setting. In this context, CpxMzd would be a representative of common magmatic processes, a less evolved precursor to more voluminous granitic intrusions, whereas AmpMzd would represent a less common magmatic record. However, before fully interpreting the record observed in Fig. 13b, the dependence of Eu/Eu* on oxygen fugacity also needs to be considered.

Europium anomaly: combined effects of oxygen fugacity, hydrous crystallization and magma composition

The degree of the Eu anomaly was proposed as an effective oxybarometer for zircon (Trail *et al.*, 2012), plagioclase (Wilke & Behrens, 1999), clinopyroxene (Fabbrizio *et al.*, 2021) and amphibole (Nandedkar *et al.*, 2016). In the studied rocks, the Eu/Eu* in zircon correlates only roughly with the values of oxygen fugacity (ΔFMQ) calculated using the oxybarometer of Loucks *et al.* (2020)

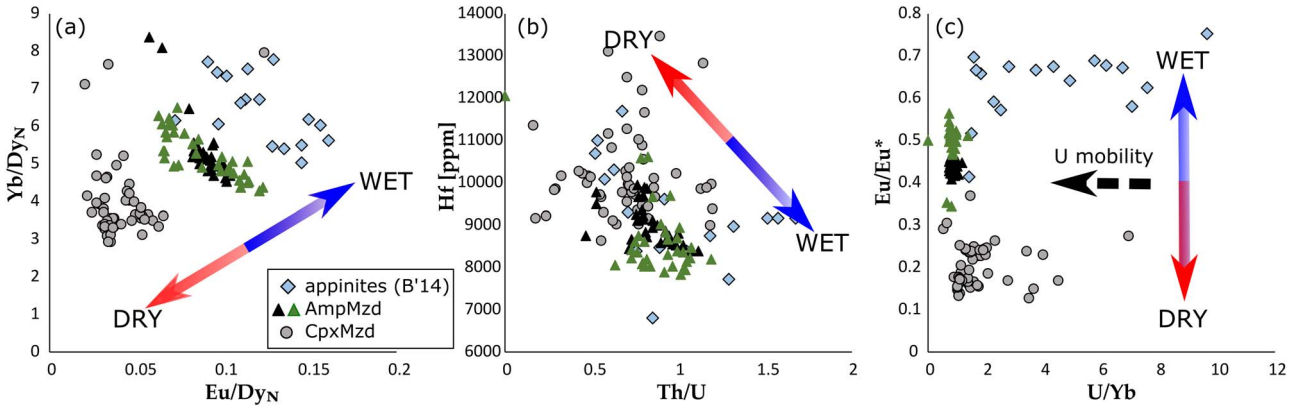

Figure 14. Diagrams showing ratios of elemental pairs in zircon that are affected by wet versus dry crystallization, approximate vector showing the expected change in zircon composition is given. Appinite zircon from Scotland (Bruand *et al.*, 2014) is shown for comparison.

based on ratios of Ce, U, and Ti in zircon (Fig. 13d). This rough correlation suggests that, although oxygen fugacity exerts some control on Eu/Eu* in zircon, it is less than that caused by plagioclase fractionation. The oxygen fugacities reconstructed from zircon (Loucks *et al.*, 2020) and amphibole (Ridolfi & Renzulli, 2012; Ridolfi, 2021) show distinct evolution with temperature for AmpMzd and CpxMzd (Fig. 13c). Data for zircon and amphibole from high-Si AmpMzd are consistent with both phases evolving slightly above the NNO buffer. On the other hand, amphibole from low-Si AmpMzd shows distinctly higher fO_2 and zircon from CpxMzd plots at fO_2 values below the NNO buffer. Such a range of fO_2 values during magma crystallization could have affected the partitioning of Eu not only for zircon but also for major phases as presented in Fig. 15. The assumption is that amphibole crystallization before plagioclase should have increased the Eu/Eu* in the melt and zircon. However, Eu/Eu* values in zircon from AmpMzd can be achieved only after Amp-dominated crystallization at fO_2 values below NNO buffer, which is in contrast to the values estimated for amphibole and partly zircon in Fig. 13c. Using the partition coefficients from Nandedkar *et al.* (2016), which fit the melt composition, oxygen fugacity and temperature estimated for AmpMzd crystallization (andesitic melt, NNO + 1, 850°C), the maximum modeled Eu/Eu* in zircon would be only 0.24 after solely amphibole crystallization, therefore, lower than that measured in zircon (Fig. 14). On the other hand, Eu/Eu* measured in zircon from CpxMzd requires Cpx and Pl-dominated fractionation at fO_2 below NNO (Fig. 15) in agreement with CpxMzd modal composition and texture as well as estimated fO_2 values for zircon (Fig. 13c). This discrepancy between measured and modeled Eu/Eu* in AmpMzd zircon indicates a more complex scenario for AmpMzd magma evolution than a simple crystallization of hydrous magma.

Amphibole monzodiorite: the record of disequilibrium and mush-fluid interaction

Figure 15 shows that high values of Eu/Eu* in zircon from AmpMzd can be reproduced only after amphibole-dominated crystallization at oxygen fugacities below NNO and such conditions are not consistent with amphibole composition in AmpMzd (Fig. 13c). Also, the occurrence of rounded plagioclase cores with high Sr content, plagioclase accumulations and euhedral plagioclase in AmpMzd are not consistent with the suppression of plagioclase crystallization. In order to reconcile the chemical evidence for delayed plagioclase crystallization in reduced conditions (fO_2 below NNO) with petrographic observations suggesting early plagioclase and chemical evidence of fO_2 above NNO, we suggest a two-stage development of AmpMzd magmas. The first stage would be the crystallization of less hydrous mafic magmas resulting in high-An plagioclase formation, together with a mafic phase, amphibole or clinopyroxene. Such a stage is consistent with the crystallization of mafic magmas (mafic underplate?) derived from melting an enriched mantle after the orogenic root delamination (Fig. 16, Janoušek & Holub, 2007). The second stage would involve the addition of hydrous fluids to these magmas (probably in the form of a crystal mush) and the melting of previously crystallized crystals resulting in the formation of a hydrous melt (Fig. 16). In this scenario, the plagioclase cores entrained in low-Si AmpMzd are remnants of the mafic magmas that were incorporated in the newly formed hydrous magma. Therefore, high-Si AmpMzd would represent hydrous magma—a product of remelting and low-Si AmpMzd—a mixture of magma and entrained crystals. Interaction between hydrous melt and clinopyroxene in the underplate could have led to clinopyroxene being replaced by amphibole. The newly produced melt would be rich in plagioclase component with Eu/Eu* not easily reproduced by one-stage fractional crystallization (Fig. 14). The two-stage scenario for AmpMzd formation would be consistent with many of the chemical peculiarities observed in zircon and apatite compositions in AmpMzd such as the lack of equilibrium between amphibole, plagioclase and whole rock. One of these peculiarities is lower temperatures yielded by the Ti-in-zircon thermometer for AmpMzd zircon than those for the CpxMzd with the temperatures for the AmpMzd being more homogeneous. Hydrous melting of a gabbroic protolith ($aH_2O = 1$) produces higher

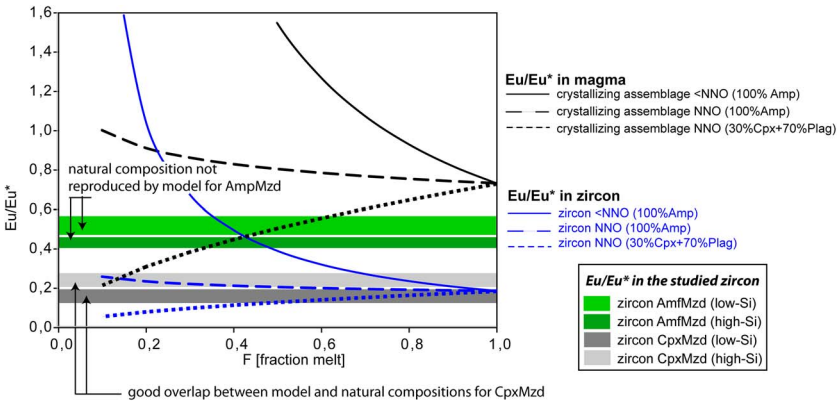

Figure 15. The model of Eu/Eu* change in magma (black lines) and co-crystallizing zircon (blue lines) for different fractionating assemblages and different oxygen fugacities during zircon crystallization (distribution coefficients for REE in zircon are from Trail *et al.*, 2012; for amphibole from Nandedkar *et al.*, 2016; for plagioclase from Wilke & Behrens, 1999, Bindeman *et al.*, 1998 and Dygert et al, 2020; for clinopyroxene from Fabbrizio *et al.* (2021). The starting composition is Eu/Eu* =0.7, which is a representative value for all the studied rocks considered as representing initial melt composition (not affected by accumulation). Crystallization of different assemblages was modeled at oxygen fugacities calculated using the oxybarometer of Loucks *et al.* (2020). Black lines show how magma composition changes depending on the crystallizing assemblage; blue lines show how zircon composition changes with the contemporaneous change in magma composition. The choice of crystallizing assemblages (i) 100% Amp and (ii) 30%Cpx + 70%Pl represents end-member scenarios for crystallization of the studied diorites, so that models for any other assemblages should plot between the currently modeled lines (100% Amp represents early amphibole crystallization, whereas 30%Cpx/70%Pl is based on modal proportions between early crystallizing Pl and Cpx in CpxMzd). The compositions of natural zircon from four diorite types are indicated as bands. The intersection of bands with modeled compositions indicates that such zircon compositions can be reproduced under conditions of crystallization. The partition coefficients and calculations complementary to the model are shown in Supplementary Material SM2.15.

volumes of melt than melting in lower water activities at similar temperatures (Koepke *et al.*, 2004). Therefore, hydrous melting could have triggered melting at lower temperatures resulting in lower Ti-in-zircon temperature values. Also, AmpMzd zircon is characterized by limited compositional variability of elements such as REE, Y, U, and Th. This limited variability is surprising as late-crystallizing zircon in mafic-intermediate systems is characterized rather by high chemical variability reflecting crystallization in isolated melt pockets (Grimes *et al.*, 2009). During hydrous melting, a composition of the newly formed melt could be buffered by the accessory phases remaining in the unmelted assemblage resulting in constant concentrations of certain elements in later crystallizing phases (Li & Hermann, 2017). A possible phase controlling REE, Y, U and Th concentrations in zircon and Y in apatite is uranothorite that occurs as euhedral, small grains in low-Si AmpMzd. Uranothorite would have crystallized during remelting as it usually forms in syenitic melts (e.g. Abdel Gawad, 2021) and, therefore, its presence may suggest that fluids that caused remelting of a mafic protolith were K-rich. Such composition of fluids is also consistent with the K-rich composition of some amphiboles in AmpMzd (Fig. 6b).

Melts crystallizing with similar proportions of plagioclase and amphibole on a peraluminous trend of hydrous magma crystallization requires temperatures of approximately 900°C (Ulmer *et al.*, 2018) and similar temperatures are suggested for the hydrous melting of the mafic underplate to produce high-Si AmpMzd. Similar conditions are also consistent with hydrous melting experiments of gabbro (Koepke *et al.*, 2004). Altogether, crystallization conditions in AmpMzd are more complex than in CpxMzd and several processes may have controlled the crystallization; however, many of them are consistent with the record of hydrous melting (see summary in Table SM3).

Local sources of magma

The Hf isotope composition of zircon is consistent with a mafic underplate derived from an enriched mantle as a viable source for the studied magmas. On the other hand, the O isotopes in zircon higher than the typical mantle values (Valley, 2018) suggest some crustal contamination of these mafic magmas. Importantly, Hf and O isotope ratios in zircon are similar in both low-Si AmpMzd and low-Si CpxMzd suggesting that the two types are derived from a similar source. Contrary to isotopic similarities between low-Si diorites, high-Si types differ in Hf isotopes but show similar ranges of O isotopic signatures. In detail, the more primitive Hf isotope composition in high-Si CpxMzd suggests the addition of mantle magma. Mantle involvement is consistent also with higher Mg, Cr and Ni whole-rock contents but not high Si in whole rock and high $\delta^{18}O$ in zircon. Alternatively, the shift in Hf isotopes and Mg, Cr and Ni in high-Si CpxMzd contents may have been caused by the melting of a heterogeneous crust. A probable source with appropriate chemical and isotopic characteristics would be a fragment of Central Sudetic Ophiolite incorporated in the crustal section probably during the earlier subduction. Similarly, a probable contaminant of high-Si AmpMzd occurs close to the intrusion since the isotopic composition of melts derived from the nearby Sowie Mountains gneisses would have lowered εHf of the contaminated AmpMzd magma and probably induced high $\delta^{18}O$ variability (εHf of Sowie granulites recalculated at 340 Ma from the εNd of O'Brien *et al.*, 1997 varies from −8 to −18). Altogether, dioritic

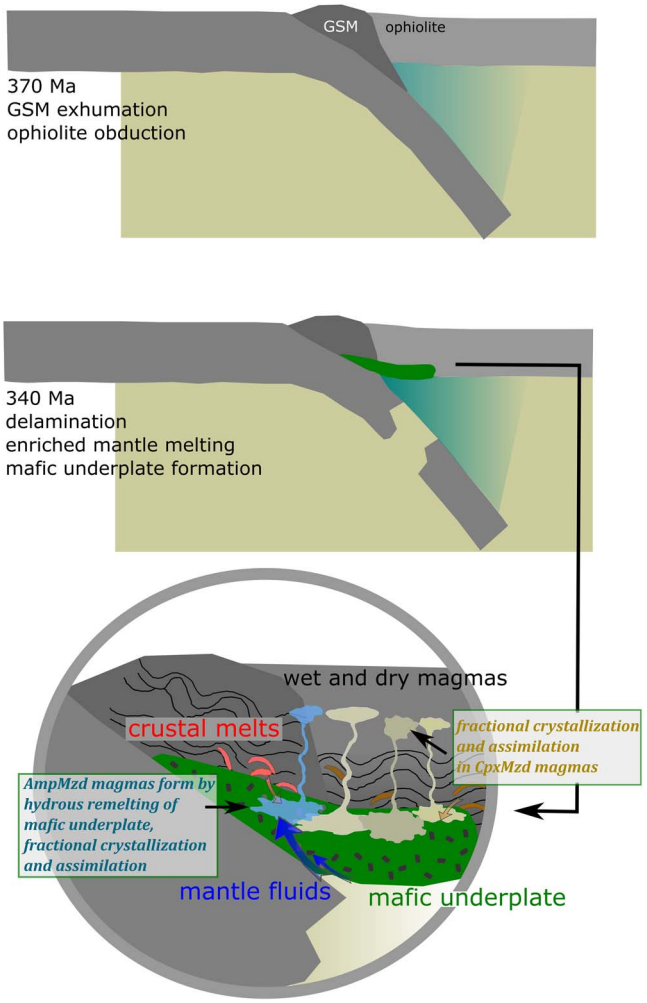

Figure 16. Schematic model of the implied tectonic setting evolution in the studied area at 370 Ma and 340 Ma. The close-up image in the circle shows details of the preferred scenario of wet and dry magma formation at 340 Ma as described in the text.

rocks record diverse differentiation processes including contamination by isotopically variable sources.

Dioritic rocks are not abundant (Collins *et al.*, 2020b); however, their relatively primitive composition records magma evolution in the MASH/MUSH zone (melting-assimilation-storage-homogenization of Hildreth & Moorbath, 1988 and mafic underplating and silicic hydration of Collins *et al.*, 2020b) that would subsequently be emplaced in the middle and upper crust. The implication is that in a post-collisional setting such rocks may provide information on the magma sources and their melting processes that are not easy to detect in granitic rocks as they were overprinted by later magmatic evolution.

Regional implications

The suggested evolution of dioritic magmas in the NZ has a bearing on tectonic interpretations in the NE Bohemian Massif. Dry and hydrous magmas were emplaced in a short-lived episode at ca. 340 Ma and complex processes and sources contributed to their formation. In the studied area, several possible magma sources were juxtaposed before 340 Ma and these included the following: (1) depleted mantle that melted at ca. 400 Ma to form the Central Sudetic Ophiolite in a supra-subduction zone setting (Awdankiewicz *et al.*, 2021; Wojtulek *et al.*, 2022), (2) an enriched mantle formed during subduction of the Góry Sowie metasedimentary rocks at ca. 400 Ma (Tabaud *et al.*, 2021) as well as (3) subducted rocks that had been exhumed to crustal depths at ca. 390–370 Ma and comprise the Góry Sowie metasedimentary rocks and probably also the Kamieniec Metamorphic Belt metasediments (Fig. 16; Jastrzębski *et al.*, 2021; Szczepański *et al.*, 2021; Tabaud *et al.*, 2021). Isotopic diversity of the studied magmas suggests a contribution from mixed mantle–crust sources or melting of a heterogeneous crust. The latter is possible, considering that the crustal section in the area contains also slices of ultramafic rocks that preserve their high Mg, Ni and Cr composition, but are affected by interaction with fluids increasing $\delta^{18}O$ (Gil *et al.*, 2022). The more primitive isotopic composition of the NZ compared with other 340 Ma magmas in the NE Bohemian Massif is best explained by the recycling of such ultramafic slices in the crustal source region, consistent with the NZ being located close to a subduction zone. Pressure estimates suggest that the NZ magmas may have been also emplaced in a deeper crust with higher contribution from mantle magmas compared with, for example, the Kłodzko-Złoty Stok Intrusion. If this was the case, currently we can observe a feeding system (AmpMzd and CpxMzd dykes) in the NZ and larger magmatic + ore associations in the Kłodzko-Złoty Stok Intrusion (Mikulski *et al.*, 2013; Jokubauskas *et al.*, 2018) with all the magmas coming from a single plutonic system, as already suggested by Oberc-Dziedzic *et al.* (2015). The age of the magmas is consistent with a rapid re-melting of the crustal section due to delamination of subducted crust (Fig. 16).

CONCLUSIONS

Wet and dry monzodioritic magmas formed within a small area in a restricted period (high-precision U–Pb zircon age of 340 Ma). Wet magmas crystallized predominately as amphibole monzodiorites and their crystallization was characterized by the delay of plagioclase saturation. However, the complex chemical composition of major and accessory minerals in wet magmas is consistent with their evolution in two stages: initial crystallization of dry magmas followed by fluid-present remelting. On the other hand, dry magmas crystallized early clinopyroxene and plagioclase during a single-stage fractional crystallization. These conditions of crystallization are reflected by zircon composition showing that zircon may be used to distinguish between wet and dry magma crystallization. We suggest that wet magmas can be distinguished by a trend on the La/Yb_{WR} to Eu/Eu^*_{zircon} plot distinct from dry magmas. Also, zircon crystallizing in

hydrous magmas has higher Eu/Dy and Yb/Dy ratios, as well as higher Hf concentrations and lower Ti-in-zircon temperatures, compared with zircon crystallizing in dry magmas. If zircon is removed from the rock representing magma composition (as antecryst) it may preserve the record of wet magma crystallization and the presence of such magmas can be implied. The distinct composition of zircon between the amphibole- and clinopyroxene-bearing rocks as well as abundant records of disequilibrium in low-Si AmpMzd samples is consistent with remelting of a mafic protolith (mafic underplate?) under fluid present conditions. Many appinities worldwide could be formed in such a process.

Hafnium and O isotopes in zircon corroborate the scenario of a single source for both wet and dry magmas with later contamination by heterogeneous crustal material. Melting of mafic underplate after delamination of subducted crust with subsequent contamination is consistent with the geological evolution of the area from 400 to 340 Ma. Altogether, monzodioritic rocks may preserve a detailed record of magma evolution and provide insight into individual processes and sources involved in crust formation that may be obliterated during massive and prolonged granite formation.

DATA AVAILABILITY STATEMENT

The data underlying this article are available in the article and in its online supplementary material.

SUPPLEMENTARY DATA

Supplementary data are available at *Journal of Petrology* online.

FUNDING

A.P. acknowledges funding from the National Science Center (Narowode Centrum Nauki) no. UMO-2013/09/B/ST10/00032. F.F. acknowledges funding from the European Union's Horizon 2020 research and innovation program under the Marie Skłodowska-Curie grant agreement no. 701494.

ACKNOWLEDGEMENTS

This paper has been a long production process punctuated by many question marks and hiatuses with new ideas blooming at regular intervals. The inspiration started with Jacek Puziewicz, but conference talks with Ewa Słaby and recent consultations with Jacek Szczepański, Magdalena Matusiak-Małek and Rafał Tyszka were also the part of the production. Tom Andersen, Robert Bolhar, Aleksandra Gawęda, Vojtěch Janoušek, and Brendan Murphy are thanked for their insightful reviews. Marlina Elburg is thanked for her careful editorial handling.

References

Abdel Gawad, A. E. (2021). Mineral chemistry (U, Th, Zr, REE) in accessory minerals from Wadi Rod Elsayalla granitoids, South Eastern Desert, Egypt. *Arabian Journal of Geosciences* **14**, 1996. https://doi.org/10.1007/s12517-021-08367-7.

Anders, E. & Grevesse, N. (1989). Abundances of the elements: meteoritic and solar. *Geochimica et Cosmochimica Acta* **53**, 197–214. https://doi.org/10.1016/0016-7037(89)90286-X.

Awdankiewicz, M., Kryza, R., Turniak, K., Ovtcharova, M. & Schaltegger, U. (2021). The Central Sudetic Ophiolite (European Variscan Belt): precise U–Pb zircon dating and geotectonic implications. *Geological Magazine*, Cambridge University Press **158**, 555–566. https://doi.org/10.1017/S0016756820000722.

Bea, F., Gallastegui, G., Montero, P., Molina, J. F., Scarrow, J., Cuesta, A. & González-Menéndez, L. (2021). Contrasting high-Mg, high-K rocks in Central Iberia: the appinite–vaugnerite conundrum and their (non-existent) relation with arc magmatism. *Journal of Iberian Geology* **47**, 235–261. https://doi.org/10.1007/s41513-020-00152-x.

Białek, D. (2020). Geochemistry and geochronology of the Jawornik granitoids, Orlica–Śnieżnik Dome, Sudetes, Poland. *Geological Quarterly* **64**, 942–957.

Bindeman, I. N., Davis, A. M. & Drake, M. J. (1998). Ion microprobe study of plagioclase-basalt partition experiments at natural concentration levels of trace elements. *Geochimica et Cosmochimica Acta* **62**, 1175–1193.

Boehnke, P., Watson, E. B., Trail, D., Harrison, T. M. & Schmitt, A. K. (2013). Zircon saturation re-revisited. *Chemical Geology* **351**, 324–334. https://doi.org/10.1016/j.chemgeo.2013.05.028.

Bonin, B., Janoušek, V. & Moyen, J.-F. (2020). Chemical variation, modal composition and classification of granitoids. *Geological Society, London, Special Publications* **491**, 9 LP–51.

Bruand, E., Storey, C. & Fowler, M. (2014). Accessory mineral chemistry of high Ba-Sr granites from Northern Scotland: constraints on petrogenesis and records of whole-rock signature. *Journal of Petrology* **55**, 1619–1651. https://doi.org/10.1093/petrology/egu037.

Cambeses, A., Molina, J. F., Morales, I., Lázaro, C., Moreno, J. A., Montero, P. & Bea, F. (2021). Compositional evolution of the Variscan intra-orogenic extensional magmatism in the Valencia del Ventoso Plutonic Complex, Ossa-Morena Zone (SW Iberia): a view from amphibole compositional relationships. *Minerals* **11**, 431. https://doi.org/10.3390/min11040431.

Cambeses, A., Montero, P., Molina, J. F., Hyppolito, T. & Bea, F. (2019). Constraints of mantle and crustal sources and interaction during orogenesis: a zircon SHRIMP U-Th-Pb and O isotope study of the 'calc-alkaline' Brovales pluton, Ossa-Morena Zone, Iberian Variscan Belt. *Lithos* **324-325**, 661–683. https://doi.org/10.1016/j.lithos.2018.11.037.

Cawood, I. P., Murphy, J. B., McCarthy, W. J. & Boyce, A. J. (2021). O and H isotopic evidence for a mantle source of water in appinite magma: an example from the late Neoproterozoic Greendale Complex, Nova Scotia. *Lithos* **386-387**, 105997. https://doi.org/10.1016/j.lithos.2021.105997.

Clemens, J. D., Stevens, G. & Mayne, M. J. (2021). Do arc silicic magmas form by fluid-fluxed melting of older arc crust or fractionation of basaltic magmas? *Contributions to Mineralogy and Petrology* **176**, 44. https://doi.org/10.1007/s00410-021-01800-w.

Collins, W. J., Huang, H. Q., Bowden, P. & Kemp, A. I. S. (2020a). Repeated S–I–A-type granite trilogy in the lachlan orogen and geochemical contrasts with a-type granites in Nigeria:

implications for petrogenesis and tectonic discrimination. *Geological Society Special Publication* **491**, 53–76.

Collins, W. J., Murphy, J. B., Blereau, E. & Huang, H.-Q. (2021). Water availability controls crustal melting temperatures. *Lithos* **402-403**, 106351. https://doi.org/10.1016/j.lithos.2021.106351.

Collins, W. J., Murphy, J. B., Johnson, T. E. & Huang, H.-Q. (2020b). Critical role of water in the formation of continental crust. *Nature Geoscience* **13**, 331–338. https://doi.org/10.1038/s41561-020-0573-6.

Condon, D. J., Schoene, B., McLean, N. M., Bowring, S. A. & Parrish, R. R. (2015). Metrology and traceability of U–Pb isotope dilution geochronology (EARTHTIME Tracer Calibration Part I). *Geochimica et Cosmochimica Acta* **164**, 464–480. https://doi.org/10.1016/j.gca.2015.05.026.

Davies, J. H. F. L., Marzoli, A., Bertrand, H., Youbi, N., Ernesto, M., Greber, N. D., Ackerson, M., Simpson, G., Bouvier, A. S., Baumgartner, L., Pettke, T., Farina, F., Ahrenstedt, H. V. & Schaltegger, U. (2021). Zircon petrochronology in large igneous provinces reveals upper crustal contamination processes: new U–Pb ages, Hf and O isotopes, and trace elements from the Central Atlantic magmatic province (CAMP). *Contributions to Mineralogy and Petrology* **176**, 9. https://doi.org/10.1007/s00410-020-01765-2.

Debon, F. & Le Fort, P. (1983). A chemical–mineralogical classification of common plutonic rocks and associations. *Transactions of the Royal Society of Edinburgh Earth Sciences* **73**, 135–149. https://doi.org/10.1017/S0263593300010117.

Dias, G., Simões, P. P., Ferreira, N. & Leterrier, J. (2002). Mantle and crustal sources in the genesis of Late-Hercynian granitoids (NW Portugal): geochemical and Sr-Nd isotopic constraints. *Gondwana Research* **5**, 287–305. https://doi.org/10.1016/S1342-937X(05)70724-3.

Dostal, J., Murphy, J. B. & Shellnutt, J. G. (2019). Secular isotopic variation in lithospheric mantle through the Variscan orogen: Neoproterozoic to Cenozoic magmatism in continental Europe. *Geology* **47**, 637–640. https://doi.org/10.1130/G46067.1.

Dostal, J., Shellnutt, J. G. & Ulrych, J. (2020). Petrogenesis of post-collisional Late Paleozoic volcanic rocks of the Bohemian Massif (Central Europe): isotopic variations of the lithospheric mantle related to Variscan orogeny. *Lithos* **354-355**, 105331. https://doi.org/10.1016/j.lithos.2019.105331.

Dygert, N., Draper, D. S., Rapp, J. F., Lapen, T. J., Fagan, A. L. & Neal, C. R. (2020). Experimental determinations of trace element partitioning between plagioclase, pigeonite, olivine, and lunar basaltic melts and an fO2 dependent model for plagioclase-melt Eu partitioning. *Geochimica et Cosmochimica Acta* **279**, 258–280. https://doi.org/10.1016/j.gca.2020.03.037.

Fabbrizio, A., Schmidt, M. W. & Petrelli, M. (2021). Effect of fO2 on Eu partitioning between clinopyroxene, orthopyroxene and basaltic melt: development of a Eu3+/Eu2+ oxybarometer. *Chemical Geology* **559**, 119967. https://doi.org/10.1016/j.chemgeo.2020.119967.

Fisher, C. M., Hanchar, J. M., Samson, S. D., Dhuime, B., Blichert-Toft, J., Vervoort, J. D. & Lam, R. (2011). Synthetic zircon doped with hafnium and rare earth elements: a reference material for *in situ* hafnium isotope analysis. *Chemical Geology* **286**, 32–47. https://doi.org/10.1016/j.chemgeo.2011.04.013.

Fowler, M. B., Kocks, H., Darbyshire, D. F. & Greenwood, P. B. (2008). Petrogenesis of high Ba-Sr plutons from the Northern Highlands Terrane of the British Caledonian Province. *Lithos* **105**, 129–148. https://doi.org/10.1016/j.lithos.2008.03.003.

Ghiorso, M. S. & Gualda, G. A. R. (2015). An H_2O-CO_2 mixed fluid saturation model compatible with rhyolite-MELTS. *Contributions to Mineralogy and Petrology* **169**, 53.

Ghiorso, M. S. & Sack, R. O. (1995). Chemical mass transfer in magmatic processes IV. A revised and internally consistent thermodynamic model for the interpolation and extrapolation of liquid-solid equilibria in magmatic systems at elevated temperatures and pressures. *Contributions to Mineralogy and Petrology* **119**, 197–212.

Gil, G., Borowski, M. P., Barnes, J. D., Jokubauskas, P., Bagiński, B., Gunia, P. & Ilnicki, S. (2022). Formation of serpentinite-hosted talc in a continental crust setting: petrographic, mineralogical, geochemical, and O, H and Cl isotope study of the Gilów deposit, Góry Sowie Massif (SW Poland). *Ore Geology Reviews* **146**, 104926. https://doi.org/10.1016/j.oregeorev.2022.104926.

Grimes, C. B., John, B. E., Cheadle, M. J., Mazdab, F. K., Wooden, J. L., Swapp, S. & Schwartz, J. (2009). On the occurrence, trace element geochemistry, and crystallization history of zircon from *in situ* ocean lithosphere. *Contributions to Mineralogy and Petrology* **158**, 757–783. https://doi.org/10.1007/s00410-009-0409-2.

Gualda, G. A. R., Ghiorso, M. S., Lemons, R. V. & Carley, T. L. (2012). Rhyolite-MELTS: a modified calibration of MELTS optimized for silica-rich, fluid-bearing magmatic systems. *Journal of Petrology* **53**, 875–890.

Guillong, M., Meier, D., Allan, M., Heinrich, C. & Yardley, B. (2008). SILLS: a MATLAB-based program for the reduction of laser ablation ICP-MS data of homogeneous materials and inclusions. *Mineralogical Association of Canada Short Course* **40**, 328–333.

Gutiérrez-Alonso, G., Murphy, J. B., Fernández-Suárez, J., Weil, A. B., Franco, M. P. & Gonzalo, J. C. (2011). Lithospheric delamination in the core of Pangea: Sm-Nd insights from the Iberian mantle. *Geology* **39**, 155–158. https://doi.org/10.1130/G31468.1.

Harrison, T. M. & Watson, E. B. (1984). The behavior of apatite during crustal anatexis: equilibrium and kinetic considerations. *Geochimica et Cosmochimica Acta* **48**, 1467–1477. https://doi.org/10.1016/0016-7037(84)90403-4.

Hawthorne, F. C., Oberti, R., Harlow, G. E., Maresch, W. V., Martin, R. F., Schumacher, J. C. & Welch, M. D. (2012). Nomenclature of the amphibole supergroup. *American Mineralogist* **97**, 2031–2048. https://doi.org/10.2138/am.2012.4276.

Heaman, L. M. (2009). The application of U–Pb geochronology to mafic, ultramafic and alkaline rocks: an evaluation of three mineral standards. *Chemical Geology* **261**, 43–52. https://doi.org/10.1016/j.chemgeo.2008.10.021.

Hildreth, W. & Moorbath, S. (1988). Crustal contributions to arc magmatism in the Andes of Central Chile. *Contributions to Mineralogy and Petrology* **98**, 455–489. https://doi.org/10.1007/BF00372365.

Hou, T., Charlier, B., Holtz, F., Veksler, I., Zhang, Z., Thomas, R. & Namur, O. (2018). Immiscible hydrous Fe-Ca-P melt and the origin of iron oxide-apatite ore deposits. *Nature Communications* **9**, 1415. https://doi.org/10.1038/s41467-018-03761-4.

Ickert, R. B., Hiess, J., Williams, I. S., Holden, P., Ireland, T. R., Lanc, P., Schram, N., Foster, J. J. & Clement, S. W. (2008). Determining high precision, in situ, oxygen isotope ratios with a SHRIMP II: analyses of MPI-DING silicate-glass reference materials and zircon from contrasting granites. *Chemical Geology* **257**, 114–128. https://doi.org/10.1016/j.chemgeo.2008.08.024.

Iveson, A. A., Rowe, M. C., Webster, J. D. & Neill, O. K. (2018). Amphibole-, clinopyroxene- and plagioclase-melt partitioning of trace and economic metals in halogen-bearing rhyodacitic melts. *Journal of Petrology* **59**, 1579–1604. https://doi.org/10.1093/petrology/egy072.

Janoušek, V., Braithwaite, C. J. R., Bowes, D. R. & Gerdes, A. (2004). Magma-mixing in the genesis of Hercynian calc-alkaline granitoids: an integrated petrographic and geochemical study of the Sázava intrusion, Central Bohemian Pluton, Czech Republic. *Lithos* **78**, 67–99. https://doi.org/10.1016/j.lithos.2004.04.046.

Janoušek, V., Gerdes, A., Vrána, S., Finger, F., Erban, V., Friedl, G. & Braithwaite, C. J. R. (2006). Low-pressure Granulites of the Lišov Massif, Southern Bohemia: Viséan metamorphism of Late Devonian plutonic arc rocks. *Journal of Petrology* **47**, 705–744. https://doi.org/10.1093/petrology/egi091.

Janoušek, V., Hanžl, P., Svojtka, M., Hora, J. M., Kochergina, Y. V. E., Gadas, P., Holub, F. V., Gerdes, A., Verner, K., Hrdličková, K., Daly, J. S. & Buriánek, D. (2020). Ultrapotassic magmatism in the heyday of the Variscan orogeny: the story of the Třebíč Pluton, the largest durbachitic body in the Bohemian Massif. *International Journal of Earth Sciences* **109**, 1767–1810. https://doi.org/10.1007/s00531-020-01872-2.

Janoušek, V. & Holub, F. V. (2007). The causal link between HP-HT metamorphism and ultrapotassic magmatism in collisional orogens: case study from the Moldanubian Zone of the Bohemian Massif. *Proceedings of the Geologists' Association* **118**, 75–86. https://doi.org/10.1016/S0016-7878(07)80049-6.

Jastrzębski, M., Budzyń, B., Żelaźniewicz, A., Konečný, P., Sláma, J., Kozub-Budzyń, G. A., Skrzypek, E. & Jaźwa, A. (2021). Eo-Variscan metamorphism in the Bohemian Massif: thermodynamic modelling and monazite geochronology of gneisses and granulites of the Góry Sowie Massif, SW Poland. *Journal of Metamorphic Geology* **39**, 751–779. https://doi.org/10.1111/jmg.12589.

Jastrzębski, M., Machowiak, K., Krzemińska, E., Lang Farmer, G., Larionov, A. N., Murtezi, M., Majka, J., Sergeev, S., Ripley, E. M. & Whitehouse, M. (2018). Geochronology, petrogenesis and geodynamic significance of the Visean igneous rocks in the Central Sudetes, northeastern Bohemian Massif. *Lithos* **316-317**, 385–405. https://doi.org/10.1016/j.lithos.2018.07.034.

Jastrzębski, M., Żelaźniewicz, A., Budzyń, B., Sláma, J. & Konečný, P. (2020). Age constraints on the pre-variscan and variscan thermal events in the Kamieniec Ząbkowicki metamorphic belt (The Fore-Sudetic Block, SW Poland). *Annales Societatis Geologorum Poloniae* **90**, 27–49. https://doi.org/10.14241/asgp.2020.05.

Jochum, K. P., Stoll, B., Herwig, K., Willbold, M., Hofmann, A. W., Amini, M., Aarburg, S., Abouchami, W., Hellebrand, E., Mocek, B., Raczek, I., Stracke, A., Alard, O., Bouman, C., Becker, S., Dücking, M., Brätz, H., Klemd, R., de Bruin, D., Canil, D., Cornell, D., de Hoog, C. J., Dalpé, C., Danyushevsky, L., Eisenhauer, A., Gao, Y., Snow, J. E., Groschopf, N., Günther, D., Latkoczy, C., Guillong, M., Hauri, E. H., Höfer, H. E., Lahaye, Y., Horz, K., Jacob, D. E., Kasemann, S. A., Kent, A. J. R., Ludwig, T., Zack, T., Mason, P. R. D., Meixner, A., Rosner, M., Misawa, K., Nash, B. P., Pfänder, J., Premo, W. R., Sun, W. D., Tiepolo, M., Vannucci, R., Vennemann, T., Wayne, D. & Woodhead, J. D. (2006). MPI-DING reference glasses for *in situ* microanalysis: new reference values for element concentrations and isotope ratios. *Geochemistry, Geophysics, Geosystems.* **7**, Q02008. https://doi.org/10.1029/2005GC001060.

Jokubauskas, P., Bagiński, B., Macdonald, R. & Krzemińska, E. (2018). Multiphase magmatic activity in the Variscan Kłodzko–Złoty Stok intrusion, Polish Sudetes: evidence from SHRIMP U–Pb zircon ages. *International Journal of Earth Sciences* **107**, 1623–1639. https://doi.org/10.1007/s00531-017-1562-x.

Kemp, A. I. S., Hawkesworth, C. J., Paterson, B. A., Kinny, P. D. & Kemp, T. (2006). Episodic growth of the Gondwana supercontinent from hafnium and oxygen isotopes in zircon. *Nature* **439**, 580–583. https://doi.org/10.1038/nature04505.

Klein, M., Stosch, H.-G. & Seck, H. A. (1997). Partitioning of high field-strength and rare-earth elements between amphibole and quartz-dioritic to tonalitic melts: an experimental study. *Chemical Geology* **138**, 257–271. https://doi.org/10.1016/S0009-2541(97)00019-3.

Koepke, J., Feig, S. T., Snow, J. & Freise, M. (2004). Petrogenesis of oceanic plagiogranites by partial melting of gabbros: an experimental study. *Contributions to Mineralogy and Petrology* **146**, 414–432. https://doi.org/10.1007/s00410-003-0511-9.

Kotková, J., Schaltegger, U. & Leichmann, J. (2010). Two types of ultrapotassic plutonic rocks in the Bohemian Massif-Coeval intrusions at different crustal levels. *Lithos* **115**, 163–176. https://doi.org/10.1016/j.lithos.2009.11.016.

Kroner, U. & Romer, R. L. (2013). Two plates - Many subduction zones: the Variscan orogeny reconsidered. *Gondwana Research* **24**, 298–329. https://doi.org/10.1016/j.gr.2013.03.001.

Kryza, R., Crowley, Q. G., Larionov, A., Pin, C., Oberc-Dziedzic, T. & Mochnacka, K. (2012). Chemical abrasion applied to SHRIMP zircon geochronology: an example from the Variscan Karkonosze Granite (Sudetes, SW Poland). *Gondwana Research* **21**, 757–767. https://doi.org/10.1016/j.gr.2011.07.007.

Kryza, R. & Pin, C. (2010). The Central-Sudetic ophiolites (SW Poland): Petrogenetic issues, geochronology and palaeotectonic implications. *Gondwana Research* **17**, 292–305. https://doi.org/10.1016/j.gr.2009.11.001.

Kubínová, Š., Faryad, S. W., Verner, K., Schmitz, M. & Holub, F. (2017). Ultrapotassic dykes in the Moldanubian Zone and their significance for understanding of the post-collisional mantle dynamics during Variscan orogeny in the Bohemian Massif. *Lithos* **272-273**, 205–221. https://doi.org/10.1016/j.lithos.2016.12.007.

Laurent, A., Janousek, V., Magna, T., Schulmann, K. & Mikova, J. (2014). Petrogenesis and geochronology of a post-orogenic calc-alkaline magmatic association: the Zulova Pluton, Bohemian Massif. *Journal of Geosciences. Prague: Czech Geological Society* **59**, 415–440. https://doi.org/10.3190/jgeosci.176.

Leake, B. E., Woolley, A. R., Arps, C. E. S., Birch, W. D., Gilbert, M. C., Grice, J. D., Hawthorne, F. C., Kato, A., Kisch, H. J., Krivovichev, V. G., Linthout, K., Laird, J., Mandarino, J., Maresch, W. V., Nickel, E. H., Rock, N. M. S., Schumacher, J. C., Smith, D. C., Stephenson, N. C. N., Ungaretti, L., Whittaker, E. J. W. & Youzhi, G. (1997). Nomenclature of amphiboles; report of the subcommittee on amphiboles of the international mineralogical association commission on new minerals and mineral names. *Mineralogical Magazine* **61**, 295–310. https://doi.org/10.1180/minmag.1997.061.405.13.

Li, H. & Hermann, J. (2017). The effect of fluorine and chlorine on trace element partitioning between apatite and sediment melt at subduction zone conditions. *Chemical Geology* **473**, 55–73. https://doi.org/10.1016/j.chemgeo.2017.10.016.

Loucks, R. R., Fiorentini, M. L. & Henriquez, G. J. (2020). New magmatic oxybarometer using trace elements in zircon. *Journal of Petrology* **61**(3), egaa034. https://doi.org/10.1093/petrology/egaa034.

Maierová, P., Schulmann, K., Lexa, O., Guillot, S., Štípská, P., Janoušek, V. & Čadek, O. (2016). European Variscan orogenic evolution as an analogue of Tibetan-Himalayan orogen: insights from petrology and numerical modeling. *Tectonics* **35**, 1760–1780. https://doi.org/10.1002/2015TC004098.

Mazur, S., Aleksandrowski, P., Kryza, R. & Oberc-Dziedzic, T. (2006). The Variscan Orogen in Poland. *Geological Quarterly* **50**, 89–118.

Melekhova, E., Blundy, J., Martin, R., Arculus, R. & Pichavant, M. (2017). Petrological and experimental evidence for differentiation of water-rich magmas beneath St. Kitts, Lesser Antilles. *Contributions to Mineralogy and Petrology* **172**, 98. https://doi.org/10.1007/s00410-017-1416-3.

Melekhova, E., Blundy, J., Robertson, R. & Humphreys, M. C. S. (2015). Experimental evidence for polybaric differentiation of primitive arc basalt beneath St. Vincent, Lesser Antilles. *Journal of Petrology* **56**, 161–192. https://doi.org/10.1093/petrology/egu074.

Mikulski, S. Z., Williams, I. S. & Bagiński, B. (2013). Early carboniferous (Viséan) emplacement of the collisional Kłodzko-Złoty Stok granitoids (Sudetes, SW Poland): constraints from geochemical data and zircon U-Pb ages. *International Journal of Earth Sciences* **102**, 1007–1027. https://doi.org/10.1007/s00531-012-0852-6.

Molina, J. F., Scarrow, J. H., Montero, P. G. & Bea, F. (2009). High-Ti amphibole as a petrogenetic indicator of magma chemistry: evidence for mildly alkalic-hybrid melts during evolution of Variscan basic–ultrabasic magmatism of Central Iberia. *Contributions to Mineralogy and Petrology* **158**, 69–98. https://doi.org/10.1007/s00410-008-0371-4.

Morimoto, N. (1988). Nomenclature of pyroxenes. *Mineralogy and Petrology* **39**, 55–76. https://doi.org/10.1007/BF01226262.

Murphy, J. B. (2013). Appinite suites: a record of the role of water in the genesis, transport, emplacement and crystallization of magma. *Earth-Science Reviews* **119**, 35–59. https://doi.org/10.1016/j.earscirev.2013.02.002.

Murphy, J. B. (2020). Appinite suites and their genetic relationship with coeval voluminous granitoid batholiths. *International Geology Review*. Taylor & Francis **62**, 683–713. https://doi.org/10.1080/00206814.2019.1630859.

Mutch, E. J. F., Blundy, J. D., Tattitch, B. C., Cooper, F. J. & Brooker, R. A. (2016). An experimental study of amphibole stability in low-pressure granitic magmas and a revised Al-in-hornblende geobarometer. *Contributions to Mineralogy and Petrology* **171**, 85. https://doi.org/10.1007/s00410-016-1298-9.

Nandedkar, R. H., Hürlimann, N., Ulmer, P. & Müntener, O. (2016). Amphibole–melt trace element partitioning of fractionating calc-alkaline magmas in the lower crust: an experimental study. *Contributions to Mineralogy and Petrology* **171**, 71. https://doi.org/10.1007/s00410-016-1278-0.

Nandedkar, R. H., Ulmer, P. & Müntener, O. (2014). Fractional crystallization of primitive, hydrous arc magmas: an experimental study at 0.7 GPa. *Contributions to Mineralogy and Petrology* **167**, 1–27. https://doi.org/10.1007/s00410-014-1015-5.

Neave, D. A. & Putirka, K. D. (2017). A new clinopyroxene-liquid barometer, and implications for magma storage pressures under Icelandic rift zones. *American Mineralogist* **102**, 777–794. https://doi.org/10.2138/am-2017-5968.

O'Brien, P. J., Kröner, A., Jaeckel, P., Hegner, E., Zelaźniewicz, A. & Kryza, R. (1997). Petrological and isotopic studies on palaeozoic high-pressure granulites, Gory Sowie Mts, Polish Sudetes. *Journal of Petrology* **38**, 433–456. https://doi.org/10.1093/petroj/38.4.433.

Oberc-Dziedzic, T., Kryza, R. & Pin, C. (2015). Variscan granitoids related to shear zones and faults: examples from the Central Sudetes (Bohemian Massif) and the Middle Odra Fault Zone. *International Journal of Earth Sciences* **104**, 1139–1166. https://doi.org/10.1007/s00531-015-1153-7.

Peccerillo, A. & Taylor, S. R. (1976). Geochemistry of eocene calc-alkaline volcanic rocks from the Kastamonu area, Northern Turkey. *Contributions to Mineralogy and Petrology* **58**, 63–81. https://doi.org/10.1007/BF00384745.

Pietranik, A. & Koepke, J. (2014). Plagioclase transfer from a host granodiorite to mafic microgranular enclaves: diverse records of magma mixing. *Mineralogy and Petrology* **108**, 681–694. https://doi.org/10.1007/s00710-014-0326-6.

Pietranik, A., Storey, C. & Kierczak, J. (2013). The Niemcza diorites and monzodiorites (Sudetes, SW Poland): a record of changing geotectonic setting at ca. 340 Ma. *Geological Quarterly* **57**, 325–334.

Pietranik, A., Storey, C., Koepke, J., Lasalle, S. & EIMF (2017). Zircon record of fractionation, hydrous partial melting and thermal gradients at different depths in oceanic crust (ODP Site 735B, South-West Indian Ocean). *Contributions to Mineralogy and Petrology* **172**, 10.

Pietranik, A. & Waight, T. E. (2008). Processes and sources during late variscan dioritic-tonalitic magmatism: insights from plagioclase chemistry (Gesiniec Intrusion, NE Bohemian Massif, Poland). *Journal of Petrology* **49**, 1619–1645. https://doi.org/10.1093/petrology/egn040.

Przybyło, A., Pietranik, A. & Zieliński, G. (2022). Cerium and Ytrium in apatite as records of magmatic processes: insight into fractional crystallization, magma mingling and fluid saturation. *Geochemistry* **82**(2), 125864. https://doi.org/10.1016/j.chemer.2022.125864.

Putirka, K. (2016). Special collection: rates and depths of magma ascent on earth: amphibole thermometers and barometers for igneous systems and some implications for eruption mechanisms of felsic magmas at arc volcanoes. *American Mineralogist* **101**, 841–858. https://doi.org/10.2138/am-2016-5506.

Puziewicz, J. (1988). Plagioclase pyroxene-biotite rock from the Kozmice quarry, Niemcza Zone (Sudetes, SW Poland): the first occurrence of vaugnerite in Polish Sudetes. *Mineralogia Polonica* **19**, 51–65.

Puziewicz, J. (1990). Amfibole oraz towarzyszące im minerały żelaza i magnezu z monzodiorytu kwarcowego z Przedborowej (Dolny Śląsk). *Archiwum Mineralogiczne (in Polish)* **45**, 61–78.

Puziewicz, J. (1992). Geneza granodiorytu z Kozmic (strefa Niemczy, Dolny Sląsk). *Archiwum Mineralogiczne (in Polish)* **47**, 95–146.

Puziewicz, J. & Mazur, S. (1995). Mylonites of the Niemcza Zone. *Annales Societatis Geologorum Poloniae* **64**, 23–52.

Ridolfi, F. (2021). Amp-tb2: an updated model for calcic amphibole thermobarometry. *Minerals* **11**, 1–9. https://doi.org/10.3390/min11030324.

Ridolfi, F. & Renzulli, A. (2012). Calcic amphiboles in calc-alkaline and alkaline magmas: Thermobarometric and chemometric empirical equations valid up to 1,130°C and 2.2 GPa. *Contributions to Mineralogy and Petrology* **163**, 877–895. https://doi.org/10.1007/s00410-011-0704-6.

Ridolfi, F., Renzulli, A. & Puerini, M. (2010). Stability and chemical equilibrium of amphibole in calc-alkaline magmas: an overview, new thermobarometric formulations and application to subduction-related volcanoes. *Contributions to Mineralogy and Petrology* **160**, 45–66. https://doi.org/10.1007/s00410-009-0465-7.

Rubatto, D. & Hermann, J. (2007). Experimental zircon/melt and zircon/garnet trace element partitioning and implications for the geochronology of crustal rocks. *Chemical Geology* **241**, 38–61. https://doi.org/10.1016/j.chemgeo.2007.01.027.

Sawicki, L. (1995) *Geological Map of Lower Silesia with Adjacent Czech and German Territories 1:100000*. Warsaw: Polish Geological Institute.

Schaltegger, U., Nowak, A., Ulianov, A., Fisher, C. M., Gerdes, A., Spikings, R., Whitehouse, M. J., Bindeman, I., Hanchar, J. M., Duff, J., Vervoort, J. D., Sheldrake, T., Caricchi, L., Brack, P. & Müntener, O. (2019). Zircon petrochronology and 40Ar/39Ar thermochronology of the Adamello Intrusive Suite, N. Italy: monitoring the growth and decay of an incrementally assembled magmatic system. *Journal of Petrology* **60**(4), 701–722.https://doi.org/10.1093/petrology/egz010.

Schaltegger, U., Ovtcharova, M., Gaynor, S. P., Schoene, B., Wotzlaw, J. F., Davies, J. F. H. L., Farina, F., Greber, N. D., Szymanowski, D. & Chelle-Michou, C. (2021). Long-term repeatability and interlaboratory reproducibility of high-precision ID-TIMS U-Pb geochronology. *Journal of Analytical Atomic Spectrometry* **36**, 1466–1477. https://doi.org/10.1039/D1JA00116G.

Schiller, D. & Finger, F. (2019). Application of Ti-in-zircon thermometry to granite studies: problems and possible solutions.

Contributions to Mineralogy and Petrology **174**, 51. https://doi.org/10.1007/s00410-019-1585-3.

Słaby, E. & Martin, H. (2008). Mafic and felsic magma interaction in granites: the Hercynian Karkonosze pluton (Sudetes, bohemian massif). *Journal of Petrology* **49**, 353–391. https://doi.org/10.1093/petrology/egm085.

Sláma, J., Košler, J., Condon, D. J., Crowley, J. L., Gerdes, A., Hanchar, J. M., Horstwood, M. S. A., Morris, G. A., Nasdala, L., Norberg, N., Schaltegger, U., Schoene, B., Tubrett, M. N. & Whitehouse, M. J. (2008). Plešovice zircon–a new natural reference material for U-Pb and Hf isotopic microanalysis. *Chemical Geology* **249**, 1–35. https://doi.org/10.1016/j.chemgeo.2007.11.005.

Streckeisen, A. (1976). To each plutonic rock its proper name. *Earth-Science Reviews* **12**, 1–33. https://doi.org/10.1016/0012-8252(76)90052-0.

Szczepański, J., Zhong, X., Dąbrowski, M., Wang, H. & Goleń, M. (2021). Combined phase diagram modelling and quartz-in-garnet barometry of HP metapelites from the Kamieniec Metamorphic Belt (NE Bohemian Massif). *Journal of Metamorphic Geology* **40**, 3–37. https://doi.org/10.1111/jmg.12608.

Tabaud, A. S., Štípská, P., Mazur, S., Schulmann, K., Míková, J., Wong, J. & Sun, M. (2021). Evolution of a Cambro-Ordovician active margin in northern Gondwana: geochemical and zircon geochronological evidence from the Góry Sowie metasedimentary rocks, Poland. *Gondwana Research* **90**, 1–26. https://doi.org/10.1016/j.gr.2020.10.011.

Tang, M., Ji, W.-Q., Chu, X., Wu, A. & Chen, C. (2020). Reconstructing crustal thickness evolution from europium anomalies in detrital zircons. *Geology* **49**, 76–80. https://doi.org/10.1130/G47745.1.

Trail, D., Bruce Watson, E. & Tailby, N. D. (2012). Ce and Eu anomalies in zircon as proxies for the oxidation state of magmas. *Geochimica et Cosmochimica Acta* **97**, 70–87. https://doi.org/10.1016/j.gca.2012.08.032.

Trubač, J., Žák, J. & Kondrová, L. (2020). Magmatic tempos in large hot orogens in comparison with continental margin arcs. *The Journal of Geology* **128**, 465–475.

Turniak, K., Mazur, S., Domańska-Siuda, J. & Szuszkiewicz, A. (2014). SHRIMP U-Pb zircon dating for granitoids from the Strzegom-Sobótka Massif, SW Poland: constraints on the initial time of Permo-Mesozoic lithosphere thinning beneath Central Europe. *Lithos* **208-209**, 415–429. https://doi.org/10.1016/j.lithos.2014.09.031.

Ubide, T., Galé, C., Larrea, P., Arranz, E., Lago, M. & Tierz, P. (2014). The relevance of crystal transfer to magma mixing: a case study in composite dykes from the central pyrenees. *Journal of Petrology* **55**, 1535–1559. https://doi.org/10.1093/petrology/egu033.

Ulmer, P., Kaegi, R. & Müntener, O. (2018). Experimentally derived intermediate to silica-rich arc magmas by fractional and equilibrium crystallization at 1·0 GPa: an evaluation of phase relationships, compositions, liquid lines of descent and oxygen fugacity. *Journal of Petrology* **59**, 11–58. 10.1093/petrology/egy017.

Valley, J. W. (2018). Oxygen isotopes in zircon. *Zircon* , 343–385.

Vervoort, J. D., Plank, T. & Prytulak, J. (2011). The Hf-Nd isotopic composition of marine sediments. *Geochimica et Cosmochimica Acta* **75**, 5903–5926. https://doi.org/10.1016/j.gca.2011.07.046.

Walker, B. A., Bergantz, G. W., Otamendi, J. E., Ducea, M. N. & Cristofolini, E. A. (2015). A MASH zone revealed: the mafic complex of the Sierra Valle Fértil. *Journal of Petrology* **56**, 1863–1896. https://doi.org/10.1093/petrology/egv057.

Warr, L. N. (2021). IMA–CNMNC approved mineral symbols. *Mineralogical Magazine* **85**, 291–320. https://doi.org/10.1180/mgm.2021.43.

Watson, E. B. & Harrison, T. M. (1983). Zircon saturation revisited: temperature and composition effects in a variety of crustal magma types. *Earth and Planetary Science Letters* **64**, 295–304. https://doi.org/10.1016/0012-821X(83)90211-X.

Watson, E. B., Wark, D. A. & Thomas, J. B. (2006). Crystallization thermometers for zircon and rutile. *Contributions to Mineralogy and Petrology* **151**, 413.

Weinberg, R. F. & Hasalová, P. (2015). Water-fluxed melting of the continental crust: a review. *Lithos* **212-215**, 158–188. https://doi.org/10.1016/j.lithos.2014.08.021.

Widmann, P., Davies, J. H. F. L. & Schaltegger, U. (2019). Calibrating chemical abrasion: its effects on zircon crystal structure, chemical composition and UPb age. *Chemical Geology* **511**, 1–10. https://doi.org/10.1016/j.chemgeo.2019.02.026.

Wiedenbeck, M., Hanchar, J. M., Peck, W. H., Sylvester, P., Valley, J., Whitehouse, M., Kronz, A., Morishita, Y., Nasdala, L., Fiebig, J., Franchi, I., Girard, J. P., Greenwood, R. C., Hinton, R., Kita, N., Mason, P. R. D., Norman, M., Ogasawara, M., Piccoli, P. M., Rhede, D., Satoh, H., Schulz-Dobrick, B., Skår, O., Spicuzza, M. J., Terada, K., Tindle, A., Togashi, S., Vennemann, T., Xie, Q. & Zheng, Y. F. (2004). Further characterisation of the 91500 zircon crystal. *Geostandards and Geoanalytical Research* **28**, 9–39. https://doi.org/10.1111/j.1751-908X.2004.tb01041.x.

Wilke, M. & Behrens, H. (1999). The dependence of the partitioning of iron and europium between plagioclase and hydrous tonalitic melt on oxygen fugacity. *Contributions to Mineralogy and Petrology* **137**, 102–114. https://doi.org/10.1007/s004100050585.

Wojtulek, P. M., Schulz, B., Klemd, R., Gil, G., Dajek, M. & Delura, K. (2022). The Central-Sudetic ophiolites—remnants of the SSZ-type Devonian oceanic lithosphere in the European part of the Variscan Orogen. *Gondwana Research* **105**, 343–365. https://doi.org/10.1016/j.gr.2021.09.015.

Woodhead, J. D. & Hergt, J. M. (2005). A preliminary appraisal of seven natural zircon reference materials for *in situ* Hf isotope determination. *Geostandards and Geoanalytical Research* **29**, 183–195. https://doi.org/10.1111/j.1751-908X.2005.tb00891.x.

Žák, J., Kratinová, Z., Trubač, J., Janoušek, V., Sláma, J. & Mrlina, J. (2011). Structure, emplacement, and tectonic setting of Late Devonian granitoid plutons in the Teplá-Barrandian unit, Bohemian Massif. *International Journal of Earth Sciences* **100**, 1477–1495. https://doi.org/10.1007/s00531-010-0565-7.

Žák, J. *et al.* (2014). A plate-kinematic model for the assembly of the Bohemian Massif constrained by structural relationships around granitoid plutons. *Geological Society, London, Special Publications* **405**, 169 LP–196.